

Magnetoconvection in a spherical shell: Equatorial symmetry during the transition from the weak- to the strong-field regime

L. J. Gostelow & R. J. Teed

Abstract

At small but supercritical Rayleigh numbers, simulations of dynamos in spherical shells often separate into two broad regimes characterised either by their relative magnetic field strength (weak/strong) or by their dominant force balance (VAC/MAC). These regimes can tend smoothly from one to the other but can also be bistable, a phenomenon which occurs particularly at large Pm. We show that in either case the transition correlates with a breaking of equatorial symmetry.

Nonlinear simulations of the geodynamo cannot be performed at accurate parameters and hence it is important to ensure that the correct (strong-field) branch is tracked as a distinguished limit is tracked towards a correct parametrisation from the simulations that we can perform. In order to understand the transition to strong-field dynamos, and better understand the mechanisms that occur in both branches, we report on a series of magnetoconvection simulations (that is, with the magnetic field fixed at the outer boundary) with which we bridge the gap between the strong- and weak-field regimes, and show that symmetry-breaking is triggered by the sudden growth of the magnetic field and in turn supports the dynamo in the strong-field regime.

1 Introduction

Dynamo simulations exhibit a wide range of solutions. Some are essentially kinematic, with the magnetic field generated by—yet only weakly influencing—the flow dynamics. Other states emerge only once the magnetic field becomes sufficiently strong. In Earth-like simulations, three principal branches are now recognised, each associated with distinct magnetic-field morphologies and strengths (Dormy et al., 2018; Dormy, 2025). These states are commonly characterised by the dominant balance between physical forces, or more precisely, in incompressible flows, by the balance between the solenoidal components of those forces (Hughes & Cattaneo, 2019; Teed & Dormy, 2023), thereby excluding pressure, which acts as a Lagrange multiplier. Although the force balance in Earth’s core is well understood, it cannot be reproduced exactly in simulations. Because force balances underpin much of the scaling and structure of dynamo behaviour (Christensen, 2010), accurately identifying subtle shifts in these balances—and their consequences for flow and field morphology—is essential for reliable extrapolation from simulations to geophysical conditions.

Nonlinear geodynamo simulations are often complemented by linear convection studies, which are computationally inexpensive and therefore provide a broader view of the families of modes that can arise. In differentially heated spheres and spherical shells, geostrophic modes onset when thermal or compositional forcing overcomes the stabilising effects of rotation and gravity; viscosity also plays a crucial role in mediating the Taylor–Proudman constraint (Roberts, 1968; Busse, 1970). The relative importance of viscous and Coriolis forces is quantified by the Ekman number, $Ek = \nu/(\Omega L^2)$, where ν is the kinematic viscosity, Ω the rotation rate, and L a characteristic length scale. Near convective onset, viscosity is the primary mediator of rotational constraints but becomes significant only at small scales; consequently, the large-scale flow is predominantly z -independent and takes the form of precessing columnar Rossby waves with heights of the order of the shell and widths scaling as $Ek^{-1/3}$, consistent with the leading-order VAC (viscous–Archimedean–Coriolis) balance. A single discrete mode typically dominates when its characteristic scale is large, suppressing the linear growth of competing modes. The precessing columns bend radially inward around the inner core, enhancing radial heat transport (Busse, 2002). Their columnar rotation, together with a thermally driven axial flow, can drive an α^2 -dynamo provided the shearing rate exceeds the rate of magnetic diffusion, usually quantified by the magnetic Reynolds number. In the VAC regime, magnetic diffusivity does not enter the leading-order force balance and its variation does not significantly alter the flow structure. Thus, one path to achieve a weak dynamo is to reduce magnetic diffusivity (i.e.,

increase the magnetic Prandtl number), though this can substantially modify the magnetic-field properties (Teed & Dormy, 2025a).

In the presence of a strong magnetic field, magnetic tension resists fluid motion that bends field lines, generally stabilising the fluid against convection. However, in rapidly rotating systems, a weak magnetic field modifies the Taylor-Proudman theorem to allow fully three-dimensional convective (magnetostrophic) modes to onset with a significantly lower critical Rayleigh number, reaching a minimum when the ratio of the Lorentz and Coriolis forces, the Elsasser number, is of order one (Chandrasekhar, 1961; Fearn, 1979). Geostrophic and magnetostrophic modes can have similar Rayleigh numbers at Elsasser numbers only just below one; when these modes coexist, the wider array of potential convective modes is thought to allow strong-field dynamos, which are essentially chaotic, with continuous turnover in the prevalence of several modes.

Sakuraba (2002) shows that polar convective modes, that is, modes which peak in amplitude inside the tangent cylinder, can have critical Rayleigh numbers similar to the geostrophic and magnetostrophic modes at order unity Elsasser numbers. Polar convective modes are distinct in that they could onset at critical Rayleigh numbers close to the values found in linear theory when convection is present, but significant only in the bulk (Gilman, 1975, 1977). Sreenivasan & Jones (2006) use an f -plane model to study these modes and show that they onset as axial plumes with oppositely signed vorticity at their upper and lower ends. Unlike (magneto)geostrophic modes, the dominant component of the flow is axial, directly supporting the poloidal magnetic field.

In a spherical shell, polar convective modes can onset with either equatorially symmetric or antisymmetric eigenfunctions with no strong preference for either (Appendix B). Equatorial symmetry is the preferred onset configuration for modes in the bulk, due to the Taylor-Proudman constraint (Busse, 1970; Sakuraba, 2002), and this symmetry is preserved by the nonlinear terms of the momentum and induction equations. The breaking of equatorial symmetry can thus be caused by the onset of polar convective modes, and the change in symmetry will significantly alter the structure of the flow. In particular, the breaking of equatorial symmetry can allow for the formation of large scale meridional circulation currents that can strengthen the poloidal magnetic field and support its reversals.

Astrophysical dynamos lie further into the diffusion-free asymptotic realm than can be reached in numerical simulation. Many studies push towards low Ek, Pm, seeking to derive scaling laws independent of ν , η , and κ , however, a refinement of this method is to push towards this asymptotic regime in an ordered way, along a distinguished limit that preserves a desired property of the simulation, such as the force balance, magnetic field morphology, or reversals. To capture these properties, at moderate Ekman numbers, it is often necessary to use larger than physical values of the magnetic or thermal Prandtl numbers (i.e., weaker than physical thermal or magnetic diffusion, e.g., Dormy, 2016; Jones & Tsang, 2025). However, at these larger values of the magnetic Prandtl number, Pm, both weak-field (columnar) and strong-field solutions can co-exist at the same input parameters. This bistability between dynamo branches means that the resultant state depends on the initial state of the flow (Dormy, 2016; Teed & Dormy, 2025a) (Bistability has also been shown to occur between the strong-field and inertia-dominated branches; Simatev & Busse, 2009; Menu et al., 2020).

One possible way to circumvent this problem of bistability is to modify the boundary conditions on the magnetic field so that it is either strengthened or weakened. The resulting simulation corresponds to magnetoconvection rather than a dynamo, but the properties of the flow are generally similar, provided that the imposed boundary conditions are consistent with those inferred from equivalent dynamo simulations (§3.2). We find that bistability occurs only for moderately strong imposed fields (4). Another advantage of magnetoconvection is that it allows for the direct determination of the influence of the magnetic field on flow, for example, by promoting convective modes with larger length scales when magnetic stresses replace viscosity as the primary mechanism that breaks the Taylor-Proudman constraint.

In this work, we use magnetoconvection simulations to study the weak- to strong-field transition. We also focus on the phenomenon of symmetry-breaking, which coincides with this transition. In §2.3, we outline the governing equations, our choice of parameterisation, and define several important output quantities, including a symmetry parameter, $s_{U/B}$, which measures the symmetry of the flow and magnetic field respectively. We then review suites of hydrodynamic and dynamo simulations from (Teed & Dormy, 2025b,a) in §3, to understand how these output quantities vary in those simulations and provide context for the results of §4, in which we present magnetoconvection simulations at three values of Pm, chosen to portray a wide array of possible phase spaces, with respect to the onset of the weak- and strong-field

branches. Finally, we summarise in §5 and, based on our results, outline a possible mechanism by which equatorial symmetry is broken.

2 Formulation

2.1 Mathematical and numerical setup

We consider a spherical shell filled with Boussinesq, electrically conducting fluid of constant density, ρ_0 , rotating at constant rate $\boldsymbol{\Omega} = \Omega \hat{\mathbf{z}}$, in spherical coordinates (r, θ, ϕ) where $r \in [R_i, R_o]$ is the radial coordinate, $\theta \in [0, \pi]$ is the colatitude, $\phi \in [0, 2\pi)$ is the azimuthal coordinate and $\hat{\mathbf{z}} = (\cos \theta, -\sin \theta, 0)$. Gravity acts radially and takes the form $\mathbf{g} = -g\mathbf{r}$, and convection is driven by a constant temperature difference ΔT , imposed at the boundaries. Diffusion is uniform and isotropic, with κ , ν , and η , the thermal, viscous, and magnetic diffusivity coefficients, respectively. The equations describing the evolution of the velocity and magnetic fields, \mathbf{u} and \mathbf{B} , and the temperature perturbation, T can be written as

$$\text{Ek} \left(\text{Pm}^{-1} \left(\frac{\partial}{\partial t} + \mathbf{u} \cdot \nabla \right) - \nabla^2 \right) \mathbf{u} = -\nabla p - 2\hat{\mathbf{z}} \times \mathbf{u} + (\nabla \times \mathbf{B}) \times \mathbf{B} + \text{PmRa}T\mathbf{r} \quad (1a)$$

$$\left(\frac{\partial}{\partial t} + \mathbf{u} \cdot \nabla - \nabla^2 \right) \mathbf{B} = \mathbf{B} \cdot \nabla \mathbf{u}, \quad (1b)$$

$$\left(\frac{\partial}{\partial t} + \mathbf{u} \cdot \nabla - \text{PmPr}^{-1} \nabla^2 \right) T = 0, \quad (1c)$$

where length has been scaled by $D = R_o - R_i$, time by D^2/η , temperature, ΔT , velocity, η/d , pressure, $\rho_0 \eta \Omega$, and magnetic field by $\sqrt{\rho_0 \mu_0 \eta \Omega}$, where μ_0 is the magnetic permeability. The scaled radial domain is $[r_i, r_o]$, and we use a standard geophysical radius ratio of $\chi = r_i/r_o = 0.35$, so that $r_i = 7/13$ and $r_o = 20/13$. The system can be described by any four independent nondimensional parameters; we use

$$\text{Ra} = \frac{g\alpha\Delta TD}{\Omega\nu r_o}, \quad \text{Ek} = \frac{\nu}{\Omega D^2}, \quad \text{Pr} = \frac{\nu}{\kappa}, \quad \text{Pm} = \frac{\nu}{\eta}, \quad (2)$$

which are the Rayleigh, Ekman, Prandtl, and magnetic Prandtl numbers, respectively. The Prandtl number is fixed at $\text{Pr} = 1$. We also fix the Ekman number, $\text{Ek} = 10^{-4}$. Although this is far from the geophysical estimate of $\text{Ek} = \mathcal{O}(10^{-15})$, it is sufficiently small to obtain rotationally dominated and interesting dynamics, but large enough to allow for a wide survey of the parameter space.

With Pr , Ek , and χ fixed, we will present results from three types of simulation: The first are hydrodynamic simulations, the equation for which can be derived from (1a)-(1c) with $\mathbf{B} \equiv \mathbf{0}$ and $\text{Pm} = 1$, where the latter criterion changes the effective nondimensionalisation, and the second are dynamo simulations for which electrically-insulating boundary conditions are used (Appendix A); these two types of simulation correspond to the same dataset as presented by Teed & Dormy (2025a,b). These are presented in §3 as motivation for and comparison with the main set of simulations: magnetoconvection simulations, in which the radial component of the magnetic field is fixed at the outer boundary (CMB), and the inner boundary (ICB) is kept with insulating conditions. Details are provided in Appendix A. The range of appropriate values for the dipolar magnetic field strength at the outer boundary, p_{10} , are chosen by comparison with the dynamo simulations and are detailed at the end of §3. In our dynamo and magnetoconvection simulations, magnetic Prandtl numbers in the range $[1, 12]$ are used, which, given the other input parameters, covers a region of parameters space that allows for different bifurcations and solution branches in dynamo solutions Teed & Dormy (2025a). In particular, large Pm values in this range admit separate weak- and strong-field dipolar branches with bistability between them and such solutions correspond to those envisaged for the distinguished limit of Dormy (2016).

With Pr , Ek , and χ fixed, and using no-slip boundary conditions, the *hydrodynamic* onset of convection occurs at the fixed Rayleigh number,

$$\text{Ra}_h \simeq 69.4, \quad (3)$$

which can be obtained from a linear stability analysis (e.g. Seeley et al., 2025). For simplicity we present our results using the supercriticality index,

$$\text{Ra}' = \text{Ra}/\text{Ra}_h, \quad (4)$$

which is defined relative to the critical Rayleigh number of the hydrodynamic ($m = 7$) onset mode. It is important to note, of course, that the true onset of (magneto)convection varies with the magnetic

field strength and the magnetic Prandtl number (Chandrasekhar, 1961). In particular, the onset of magnetoconvection is reduced when $\Lambda \gtrsim \text{Ek}^{1/3}$, reaching a minimum when $\Lambda \simeq \mathcal{O}(1)$; that is, when a balance is reached between the reduction of the geostrophic (Taylor-Proudman) constraint, which is destabilising, and the stabilising effect of magnetic tension (Fearn, 1979; Sakuraba, 2002; Jones et al., 2003).

2.2 Output quantities

The Elsasser number measures the relative sizes of the Lorentz and Coriolis forces. In rapidly rotating systems, for which the Coriolis force is an essential part of the dominant balance, the Elsasser number is expected to be of order unity if the Lorentz force is also part of the dominant balance. The Elsasser number is traditionally approximated as the square of the non-dimensional magnetic field strength,

$$\frac{|\langle \mathbf{j} \times \mathbf{B} \rangle|}{2\rho |\langle \boldsymbol{\Omega} \times \mathbf{u} \rangle|} \sim \Lambda = \frac{\langle B \rangle^2}{2\rho\mu\eta\Omega}, \quad (5)$$

where $\langle \cdot \rangle$ denotes a suitable measure of size, chosen here as $\langle \cdot \rangle = \left(\int_V |\cdot|^2 dV \right)^{1/2}$, which is the L_2 norm. It has been noted (e.g. Soderlund et al., 2012; Dormy, 2016) that this quantity is order unity for both weak- and strong-field solutions, and therefore suggests that a more refined estimate is,

$$\Lambda' = \frac{\langle B \rangle^2}{2\Omega\mu\rho \langle U \rangle \ell_\eta} = \Lambda \frac{L}{\text{Rm}\ell_\eta}, \quad (6)$$

where $\text{Rm} = \langle U \rangle D/\eta$ is the traditional magnetic Reynolds number and

$$\ell_\eta^2 = \frac{\langle \mathbf{B} \rangle^2}{\langle \mathbf{j} \rangle^2} \quad (7)$$

is the magnetic diffusion scale, which is the scale at which Ohmic dissipation occurs and thus determines the strength of the magnetic field through power balance when viscous energy losses are negligible (e.g. Oruba & Dormy, 2014). Using Λ' gives a more refined estimate of the dominant balance and generally captures the difference between weak- and strong-field solutions (Teed & Dormy, 2023); an even more accurate estimate of the balance can be found by directly calculating the forces or their curls (Teed & Dormy, 2025b).

In our magnetoconvection work, since the magnetic field is partly controlled at the boundary and may be artificially strong or weak (as required), we introduce a modified Elsasser measure,

$$\Lambda'_{-as} = \frac{\langle B \rangle_{m \neq 0}^2}{2\Omega\mu\rho \langle U \rangle \ell_\eta} \leq \Lambda', \quad (8)$$

in which the axisymmetric component of the magnetic energy is eliminated. We find that Λ'_{-as} provides a useful method for measuring the influence of the small-scale magnetic field in magnetoconvection simulations, especially when used in concert with Λ' and the known input magnetic field strength.

A key change in the flow at weak nonlinearity as thermal forcing is increased and convection becomes more vigorous is the breaking of the Taylor-Proudman constraint, that is, the trend away from a largely z -invariant flow. Soderlund et al. (2012) suggest that the anisotropy of such a flow can be measured by its columnarity, the relative size and z -independence of the z -component of the vorticity. We calculate this as

$$C_{\omega z} = \frac{\langle h^{-1/2} |\int_z \omega'_z| \rangle}{\langle \boldsymbol{\omega}' \rangle}, \quad (9)$$

where $h = 2\sqrt{r_0^2 - s^2}$ and $\boldsymbol{\omega}'$ corresponds to the vorticity after the zonal flow (the axisymmetric component of $\boldsymbol{\omega}$) is removed. The norm in the numerator only integrates over the remaining two dimensions, s and ϕ , for $s \in [r_i, r_o]$, outside the tangent cylinder. This measure is also used by Mason et al. (2022) who define it in a qualitatively similar way. If \mathbf{u} is non-zero, then $C_{\omega z}$ is therefore a scalar which will vary between a third, for isotropic flow, and almost unity, for flow which is z -independent except in boundary layers where some z -independence is essential.

We also define a parameter, s , that reports the mirror symmetry of \mathbf{u} and \mathbf{B} about the equator,

$$s_u = \frac{\langle \mathbf{u}_s \rangle - \langle \mathbf{u}_{as} \rangle}{\langle \mathbf{u}_s \rangle + \langle \mathbf{u}_{as} \rangle}. \quad (10)$$

where

$$\mathbf{u}_s = \frac{\mathbf{u}(\theta) + \mathbf{u}^r(\pi - \theta)}{2} \quad \mathbf{u}_{as} = \frac{\mathbf{u}(\theta) - \mathbf{u}^r(\pi - \theta)}{2}, \quad (10a,b)$$

and \mathbf{u}^r denotes the reflection of \mathbf{u} across the equator. The equivalent for the magnetic field, s_B , can also be defined similarly. s lies in the range $[-1, +1]$ where $+1$ corresponds to a perfectly equatorially symmetric vector field and -1 to a perfectly anti-symmetric one. An equivalent definition is to calculate $\langle u_s \rangle$ from the energy of the poloidal modes with $l - m$ even and the toroidal modes with $l - m$ odd; \mathbf{u}_{as} is then the remainder of the total energy.

Finally, we also consider a separation of the kinetic energy into its components perpendicular and parallel to the rotation axis, as well as the zonal component. These are defined by

$$\text{KE}_{\text{zonal}} = \frac{1}{2} \langle (u_\phi)_{m=0} \rangle^2, \quad (11a)$$

$$\text{KE}_{\parallel} = \frac{1}{2} \langle u_z \rangle^2, \quad (11b)$$

$$\text{KE}_{\perp} = \frac{1}{2} \langle |\mathbf{u}| \rangle^2 - \text{KE}_{\text{zonal}} - \text{KE}_{\parallel}, \quad (11c)$$

2.3 Minimal field configuration

In the magnetoconvection setup, the ICB is assumed to be electrically insulating, whilst the field at the outer boundary is specified so that

$$\hat{\mathbf{r}} \cdot \mathbf{B} = \frac{2C}{r_o} \cos \theta \hat{\mathbf{r}} \quad (12)$$

where $C = p_{10}$ (Appendix A). Two possible divergence- and curl-free solutions are a uniform axial field

$$\mathbf{B} = \frac{2C}{r_o} \hat{\mathbf{z}}, \quad (13)$$

and a dipolar field,

$$\mathbf{B} = \frac{r_o^2 C}{r^3} \left(2 \cos \theta \hat{\mathbf{r}} + \sin \theta \hat{\boldsymbol{\theta}} \right). \quad (14)$$

The total (dimensional) magnetic energy is given by

$$\text{ME}^* = \rho \eta^2 D \frac{\text{Pm}}{\text{Ek}} \int_V \frac{B^2}{2} dV, \quad (15)$$

where V corresponds to the simulated domain, the spherical shell. Hence, the non-dimensional magnetic energy is

$$\text{ME} = \frac{\text{Pm}}{\text{Ek}} \int_V \frac{B^2}{2} dV. \quad (16)$$

For the two magnetic field solutions (13) and (14), the expression for the magnetic energy is:

$$\text{ME}_{\text{axial}} = C^2 \frac{\text{Pm}}{\text{Ek}} \frac{8\pi}{r_o^3} (r_o^3 - r_i^3), \quad (17)$$

$$\text{ME}_{\text{dip}} = C^2 \frac{\text{Pm}}{\text{Ek}} \frac{4\pi r_o^4}{3} (r_i^{-3} - r_o^{-3}). \quad (18)$$

The energy of the axial magnetic field is smaller for $\chi < 0.394$ and hence for $\chi = 0.35$ the axial field configuration is preferred. For example, in the case $\text{Pm} = 1$, $\text{Ek} = 10^{-4}$, $C = 1.0$ (cf. Figure 5m), we have

$$\text{ME}_{\text{axial}} = 1.23 \times 10^5, \quad (19)$$

$$\text{ME}_{\text{dip}} = 1.44 \times 10^6. \quad (20)$$

The poloidal magnetic energy in these simulations is $ME \approx 1.3 \times 10^5$, which corresponds closely with an axial magnetic field.

Pm	1	2	5	12	25
Ra'	4.82	3.7	2.7	2.03	1.4
Rm	45.5	67.5	112	205	190

Table 1: Time-averaged value of the magnetic Reynolds number, $\overline{\text{Rm}}$, for Rayleigh numbers, Ra , just above the onset of dynamo action in dynamo (electrically insulating outer boundary) simulations at a range of magnetic Prandtl numbers, Pm ($\text{Pr} = 1$, $\text{Ek} = 10^{-4}$). For $\text{Pm} = 1, 2, 5, 12$ the flow and magnetic fields correspond to a weak-field dipolar solution, whilst the $\text{Pm} = 25$ case corresponds to a hemispherical dynamo - see Teed & Dormy (2025b).

approximated by

$$C_{\omega z} \sim \frac{2U_{\perp}/\ell_{\perp}}{2U_{\perp}/\ell_{\perp} + U_{\parallel}/\ell_{\parallel}} = \frac{2}{2 + \frac{U_{\parallel}}{U_{\perp}} \frac{\ell_{\perp}}{\ell_{\parallel}}}, \quad (22)$$

where $U_{\parallel}/U_{\perp} \approx \sqrt{0.2}$ can be determined from the energy balance (Figure 1c), and we can take $\ell_{\parallel} = 2\sqrt{r_o^2 - s_c^2}$, the height of the sphere at the critical radius, $s_c \approx 0.42r_o$, and $\ell_{\perp} = 2s_c\pi/m_c$, where $m_c = 7$ is the mode of onset. Using these, we can obtain an estimate of $C_{\omega z} \approx 0.955$, which is slightly larger than the value calculated directly. As the Rayleigh number increases, the flow becomes unstable further away from the critical radius and the convective columns increase their radial extent, slightly increasing ℓ_{\perp} , and therefore slightly decreasing $C_{\omega z}$. The onset modes are equatorially symmetric (Busse, 1970), and hence the flow remains equatorially symmetric since the nonlinear terms preserve this symmetry (Figure 1b); antisymmetric modes must onset separately.

Increasing the Rayleigh number above $\text{Ra}' = 2$ eventually leads to an instability of the axial columns which results in a steady decline in $C_{\omega z}$; this also allows other modes to grow and eventually dominate over the primary onset mode. The columnarity, Figure 1a, can also be compared with Figure 3a of Soderlund et al. (2012), who use $\chi = 0.4$, i.e. a slightly larger inner core radius, and $\text{Ek} \approx 1.7 \times 10^{-4}$ †. This leads to a more rapid decrease in $C_{\omega z}$ with Ra' since the preferred azimuthal wavenumber of convection, m_c , grows due to the larger inner core (e.g. Seeley et al., 2025), and hence convective columns become unstable to centrifugal instabilities at lower Ra' .

At $\text{Ra}' \approx 10$ the symmetry, s_u , suddenly decreases due to the convective onset of equatorially antisymmetric modes. Gilman (1977) describes a similar situation for the solar convection envelope; since the eigenfunction of the equatorially symmetric onset mode, and hence the resultant convection columns, are localised to the region outside the tangent cylinder, the polar modes, whose eigenfunctions peak inside the tangent cylinder, onset at approximately the same Rayleigh number as expected from linear theory; meanwhile, the non-dominant equatorial modes are strongly suppressed by the $m_c = 7$ mode and onset well beyond the linear value. Gastine & Aurnou (2023) have also raised the importance of the polar mode, discussing it in the context of significantly increasing Nu , the heat flux; this occurs since convection cells can develop in the tangent cylinder whose radial flow is less affected by the Coriolis force. We shall see later that this increased radial flow also affects the generation of the poloidal field. The lack of a jump in $C_{\omega z}$ at $\text{Ra}' = 10$, which, unlike s_u , is calculated only over the region outside the tangent cylinder, supports the idea that the antisymmetric instability onsets inside the tangent cylinder.

3.2 Dynamo models

When a magnetic seed field is added to hydrodynamic convection, then it can be amplified provided that the magnetic Reynolds number, Rm , is sufficiently large (Dormy & Soward, 2007). Table 1 shows the Rayleigh numbers Ra' , and the magnetic Reynolds numbers at the onset of dynamo action for a range of Pm . At Ra' close to unity, the flow is largely columnar (Figure 4a,4b) and this symmetry seems to increase the Rm required for the dynamo mechanism to operate. After onset, the columnar dynamo mechanism is straightforward in that the effect of the axial and columnar flows can be de-coupled and play a role in generating the poloidal or toroidal field, respectively (Jones, 2011). The growth of the magnetic field leads to an increase in Ohmic diffusion and hence the saturation of the magnetic field can be determined from the limitations of the energy balance; the magnetic field strength saturates once it significantly reduces

†Soderlund et al. (2012) use $\text{Ek} = 10^{-4}$, but define their Ekman number as $\text{Ek} = \nu/2\Omega D^2$, where D is the distance between the outer and inner boundaries and also use $\chi = 0.4$; one way to convert is to fix r_o , the outer radius, which gives the scale factor $2 \times (1 - 0.4)^2 / (1 - 0.35)^2 \approx 1.7$.

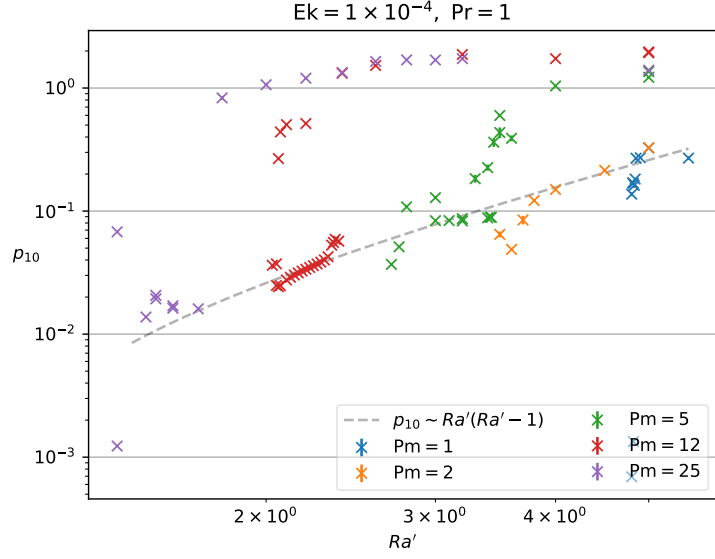


Figure 2: The $(l, m) = (1, 0)$ component of the poloidal scalar, p_{10} , at the outer boundary, for dynamo simulations with varied Pm and Ra' close to the onset of (hydrodynamic) convection. (This data is derived from simulations conducted by Teed & Dormy (2025b,a)).

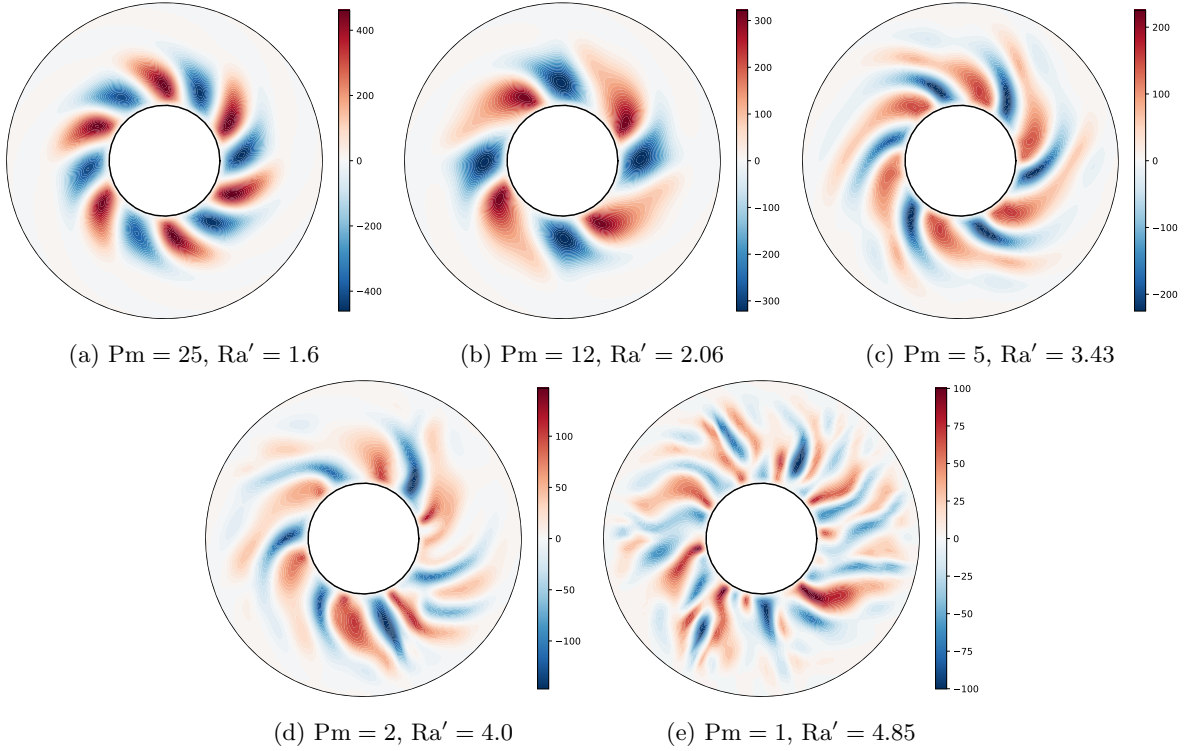


Figure 3: u_r/Pm for dynamo simulations in the “weak-field” regime, just above the onset of dynamo action.

the amplitude of the velocity, hence $B \sim U$. Combining this with (21) gives the estimate

$$p_{10} \sim \text{Ra}' (\text{Ra}' - 1), \quad (23)$$

which is overlaid as a dashed line on Figure 2. This is too weak to significantly alter the morphology of the flow, although it can adjust the preferred mode, as in Figure 3a, 3b, which are dominated by $m = 6$ and $m = 4$ modes, respectively, as opposed to the preferred hydrodynamic onset mode of $m = 7$. This saturation amplitude is almost independent of Pm , whilst dynamo onset is not, and so, whilst dynamo onset can occur almost arbitrarily close to $\text{Ra}' = 1$ by increasing Pm , the saturated magnetic field strength should tend to zero in that limit. However, it has also been hypothesised that a subcritical dynamo, in which dynamo action occurs at Rayleigh numbers below hydrodynamic onset, could be possible since the onset of convection can be decreased by a sufficiently large magnetic field. Fearn (1979) predicts that for asymptotically small Ek , $p_{10} \sim B_0 \gtrsim \mathcal{O}(\text{Ek}^{1/6})$ should be large enough to begin to decrease Ra_c . Mason et al. (2022) find that $\text{Ek} = 10^{-4}$ is not sufficiently small to be asymptotic and that a larger field, $B_0 = \mathcal{O}(1)$ is required to alter Ra_c (and also depends on Pm). These scalings are not amenable to the search for a subcritical dynamo.

Figure 2 shows that $p_{10} \approx 1 - 2$ on the strong-field branch (Dormy, 2016), where the saturation of the magnetic field strength is now determined by a dominant MAC balance (Teed & Dormy, 2025a). Thus, a strong-field is essential for the existence of this state, opening up the possibility of bistability between weak- and strong-field dipolar branches, which can be clearly seen in Figure 2 and generally, for a range of $\text{Pm} \gtrsim 5$ (Teed & Dormy, 2025b).

As the Rayleigh number increases ($\text{Ra}' \gtrsim 5$), inertia grows and convective rolls can become unstable to centrifugal instabilities. This characterises the onset of inertia-dominated solutions; these solutions can also sustain a magnetic field (for sufficiently large Pm), although they have a tendency to be multipolar rather than dipolar due to the smaller inertial(/Coriolis) scales (compared with the (VAC) onset scales). However, the length scales on the strong-field dipolar (MAC) branch are larger since the magnetic field can overcome the resistance of large length scales perpendicular to the rotation axis from the Coriolis effect. The larger length scales on this branch reduce the energy lost to diffusion and hence increase the strength of the dipolar field; this feedback mechanism is another potential avenue for bistability.

The energy in zonal flow, which is on par with the other two components in hydrodynamic convection, is found to drop significantly in dynamo simulations, since it is resisted by the presence of a large scale poloidal field (Aubert, 2005). We investigate this aspect of the problem in §4, in our range of magnetoconvection simulations. In the absence of a significant Ω -effect from a zonal flow, the dynamo mechanism on all three branches must be of an α^2 -type. A straightforward balance shows that the toroidal component of the field should therefore be of comparable strength to the poloidal field (Roberts & Soward, 1992). Teed & Dormy (2025b) verify this in the strong-field regime, but find that the toroidal field can be several times larger in the weak-field regime; a feature that can perhaps be explained by the disparity between the strengths of the axial and columnar flows in that case.

Figure 4 shows the columnarity and symmetry in dynamo simulations for Ra' between the onset of dynamo action and $\text{Ra}' = 5$ for the two values of Pm that exhibit the clearest bistability between weak- and strong-field (dipolar) solutions. The sharp drops in equatorial symmetry at $\text{Ra}' = 3.3$, for $\text{Pm} = 5$, and $\text{Ra}' = 2.1$, for $\text{Pm} = 12$, indicate that an important element in the onset of strong-field convection is the breaking of equatorial symmetry which, as in hydrodynamic convection, seems to occur due to the destabilisation of antisymmetric modes of convection. Polar convective modes are significantly destabilised by the presence of an axial magnetic field since the wavelength of the onset mode perpendicular to the rotation axis is short, minimising the effect of rotation, which is felt more strongly inside the tangent cylinder; this also corresponds to the form required to minimise the bending of axial field lines (Sakuraba, 2002). The columnarity drops at the onset of the polar modes due to the growth of the magnetic field which can then destabilise convective rolls in the flow outside the tangent cylinder.

With our magnetoconvection simulations we aim to replicate the strength of the radial magnetic field on the outer boundary separately for weak- and strong-field solutions. Thus, to determine the appropriate magnetic field strength to apply in magnetoconvection simulations, we refer to Figure 2, which shows the value of p_{10} (the $(l, m) = (1, 0)$ component of the poloidal scalar) at the outer boundary in a set of dynamo simulations. To represent the weak-field dipolar solution branch we choose $p_{10} = 0.1$, although, as we will see, we can still reach the strong-field dipolar branch with this boundary condition with sufficiently large Pm , Ra' . For the strong-field dipolar branch, we see that p_{10} generally lies in the range $(3 \times 10^{-1}, 2 \times 10^0)$, and increases with Ra' and Pm . We choose to use $p_{10} = 0.5$ and $p_{10} = 1$ to reflect the strong-field branch.

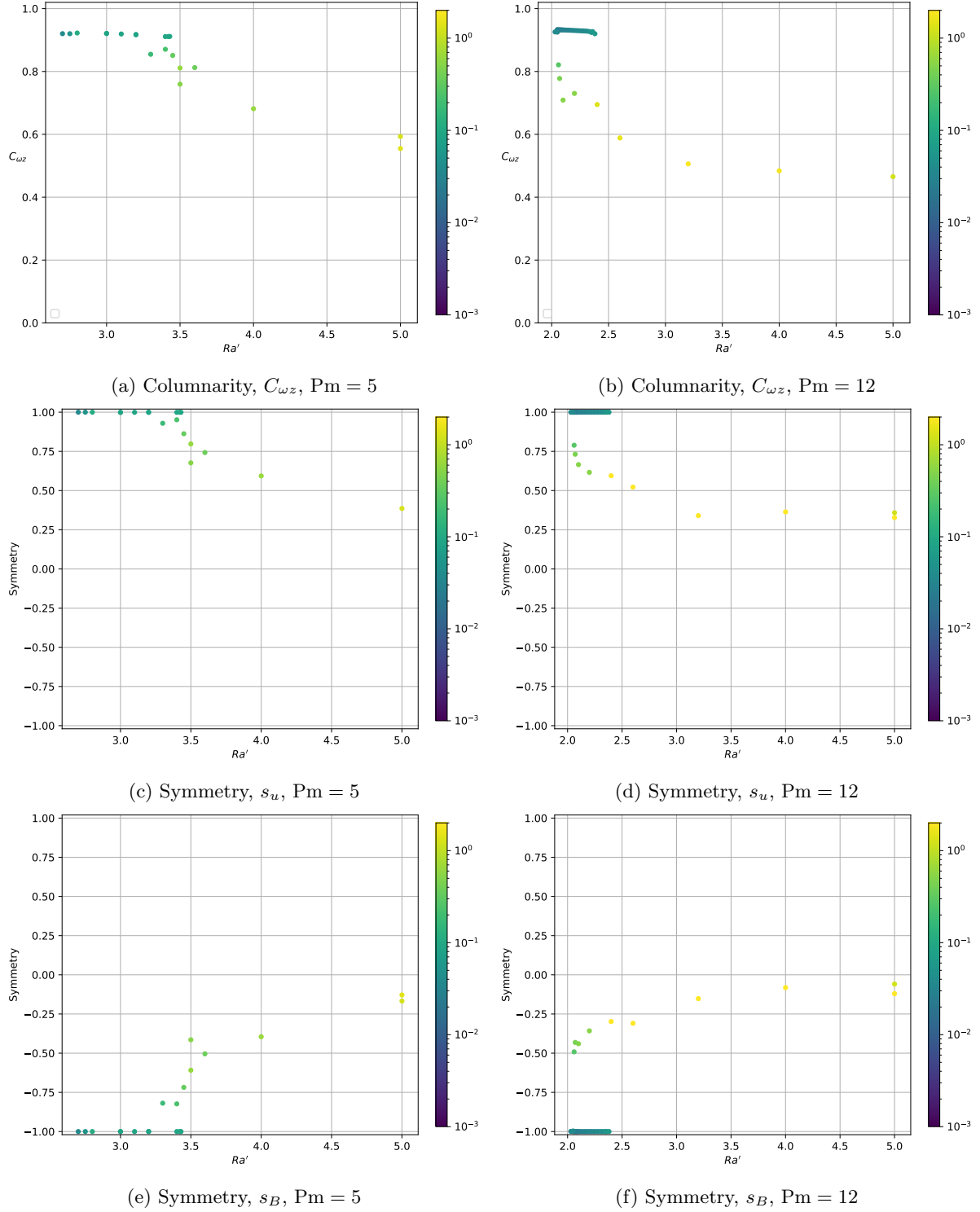


Figure 4: Global diagnostics of dynamo simulations for $Pm = 5, 12$ and $Ra' \in (1, 5]$ where points are coloured by $p_{10}(r = r_o)$: (a-b) Columnarity (equation 9); Symmetry (equation 10) of the flow (c-d) and field (e-f).

4 Magnetoconvection simulations

In this section, we present results from magnetoconvection simulations at $\text{Pm} = 1, 5, 12$ with fixed $\text{Ek} = 10^{-4}$, $\text{Pr} = 1$, Rayleigh numbers $\text{Ra}' \in (1, 5]$, and imposed axial field strengths $p_{10} \in [0.0, 2.5]$. Figure 5 summarises the global diagnostics across this parameter space, including columnarity, equatorial symmetry of the flow and magnetic field, and the total kinetic and magnetic energies.

Figures 5a–5c show the columnarity $C_{\omega z}$ of the bulk flow outside the tangent cylinder. Values close to unity correspond to nearly z -independent, columnar convection, while $C_{\omega z}$ would indicate fully three-dimensional isotropic flow. Across the entire series we find $C_{\omega z} \gtrsim 0.5$, indicating that rotational constraints remain dynamically important throughout the parameter range. However, increasing either Pm or the imposed field strength reduces columnarity, indicating that the Lorentz force, particularly that associated with the small-scale magnetic field, can relax the Taylor–Proudman constraint.

Figures 5d–5i show the equatorial symmetry of the velocity and magnetic fields. The flow remains predominantly equatorially symmetric ($s_u > 0$) for all cases considered, consistent with the persistence of rotational control. As Ra' increases, s_u approaches an apparent asymptotic value near $s_u \approx 1/3$, although confirmation of this behaviour would require access to higher Rayleigh numbers. Increasing either Pm or p_{10} substantially lowers the Rayleigh number at which equatorially asymmetric states become accessible, compared with the hydrodynamic case where symmetry breaking occurs only for $\text{Ra}' \approx 10$ (Figure 1b).

The magnetic field is largely equatorially antisymmetric ($s_B < 0$), reflecting both the imposed boundary conditions and the symmetry of the dominant convective modes. Perfect antisymmetry occurs when the flow itself is perfectly symmetric (i.e. at low Ra'). In asymmetric states, s_B approaches a limiting value near $s_B \approx -0.2$, with the rate of convergence depending strongly on Pm and, for small Pm , on the imposed field strength. This is quite close to zero, which may seem surprising given the boundary field is purely antisymmetric, but indicates the importance of the onset of the antisymmetric modes on the morphology of the magnetic field.

The kinetic and magnetic energies exhibit a more complex dependence on Ra' , Pm , and p_{10} . At small Ra' the kinetic energy is small and the magnetic energy is dominated by the imposed poloidal field (§2.3), and as Ra' increases both energies increase monotonically. Several sharp changes in both kinetic and magnetic energies coincide with the loss of equatorial symmetry and signal transitions between distinct flow regimes. These transitions are examined in detail for each value of Pm in the following subsections.

4.1 Magnetoconvection with $\text{Pm} = 1$

At $\text{Pm} = 1$, the system lies only slightly above the threshold for self-sustained dynamo action, with dynamo solutions appearing only for $\text{Ra}' \gtrsim 4.4$ (Figure 2). Over the Rayleigh number range considered here, the magnetic field is therefore primarily controlled by the imposed axial field, particularly for $p_{10} = 1.0$. For all values of p_{10} examined at $\text{Pm} = 1$, we find a single continuous branch of magnetoconvection solutions, with no evidence of bistability or hysteresis.

For weak imposed fields ($p_{10} = 0.1$), the Lorentz force remains subdominant relative to the Coriolis, viscous, and buoyancy forces, and the flow closely resembles the hydrodynamic columnar state. The preferred azimuthal mode is $m = 7$, columnarity is only slightly reduced relative to the hydrodynamic case (Figure 5a), and the flow remains equatorially symmetric throughout the explored range of Ra' (Figure 5d). As Ra' increases, inertial effects strengthen while viscous contributions weaken, with approximate parity between inertia and viscosity reached near $\text{Ra}' = 4.85$, where inertia slightly dominates at low orders and viscosity at high orders due to its additional derivative (Figure 6e).

For $p_{10} = 1.0$ the field is dominated by the imposed poloidal field and in the range of Ra' shown, the energy of the toroidal magnetic field does not grow as large as the poloidal energy, although it increases significantly as Ra' increases. At $\text{Ra}' = 1.3$, the flow takes a form similar to the hydrodynamic columns and remains largely z -independent (as indicated by $C_{\omega z}$ in Figure 5a). The imposed magnetic field is weakly swept by the columnar flow and is strongest in the cold, inward, convective plumes (Figures 7a,b). The force balance for this run is shown in top row of Figure 6. Odd and even l -modes are shown separately because the strong equatorial symmetry of the buoyancy force suppresses odd- l contributions at low Rayleigh number, particularly when the convective onset mode has m even (here $m = 8$ is preferred). The Lorentz force is large at small l due to the imposed field and still large, but on par with the viscous force for all orders $l \geq 8$ (the onset mode); at the smallest orders, $l \gtrsim 32$, inertia becomes larger than the Lorentz force.

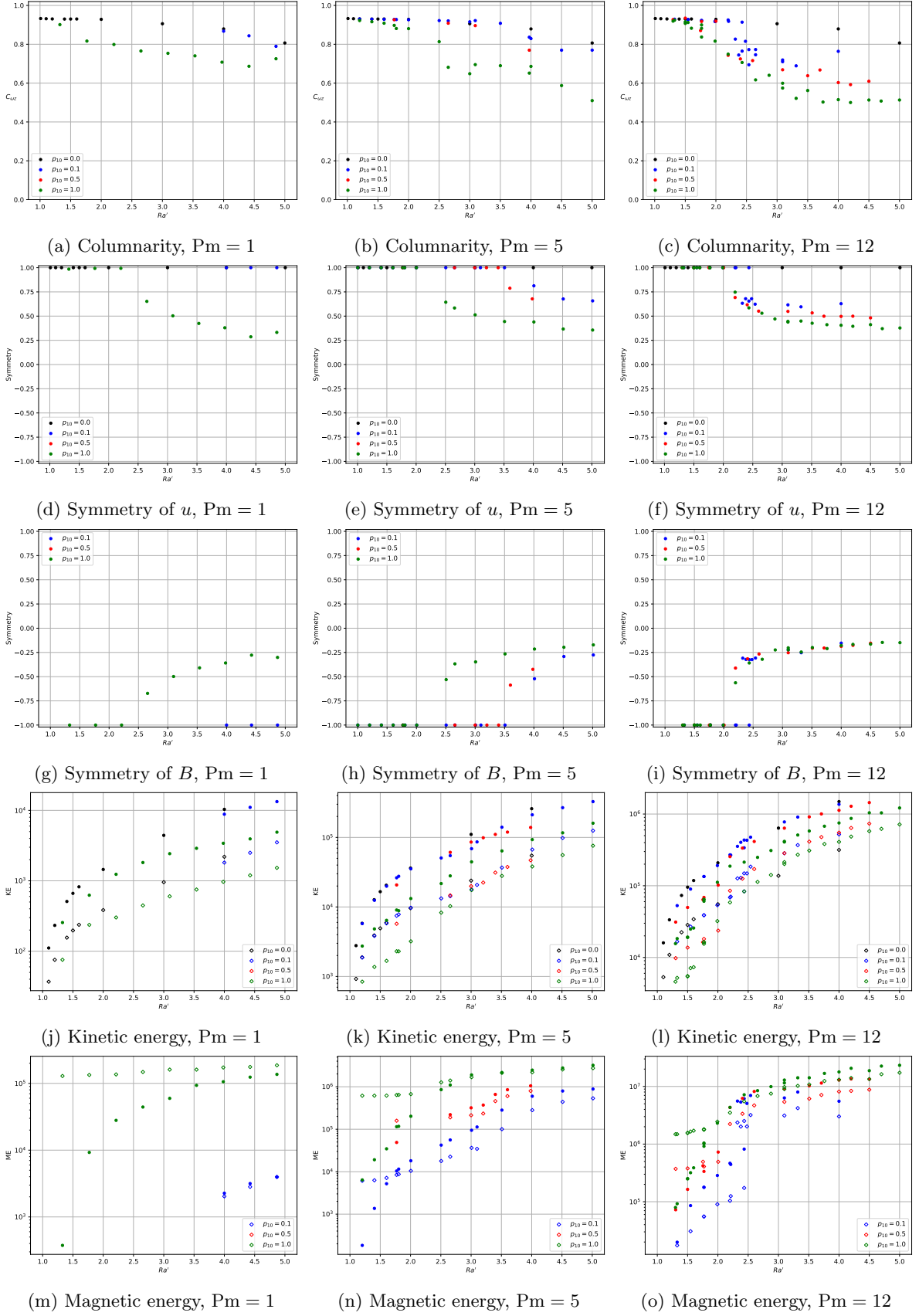


Figure 5: Global diagnostics of magnetoconvection simulations for varied Pm , p_{10} and Ra' in the range $(1, 5]$: (a-c) Columnarity (equation 9); Symmetry (equation 10) of the flow (d-f) and field (g-i); Total poloidal (unfilled diamonds) and toroidal (filled circles) of the magnetic energy (j-l) and kinetic energy (m-o). Black points refer to hydrodynamic simulations which are independent of Pm , but note that the kinetic energy is rescaled by a factor of Pm^2 to use strong-field non-dimensionalisation.

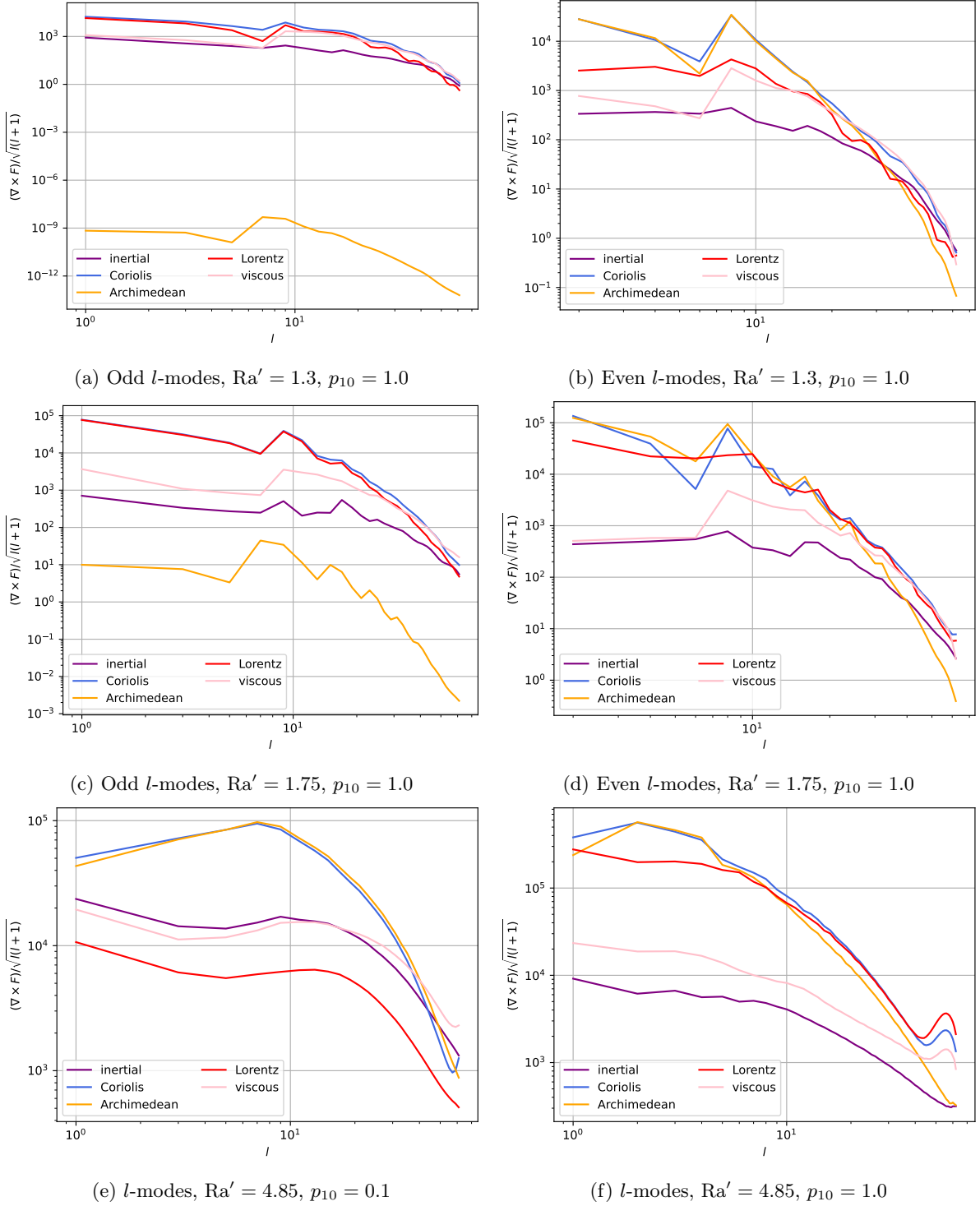


Figure 6: Time-averages of the compensated-curl of forces in simulations at $Pm = 1$, $p_{10} = 0.1, 1.0$, at three values of Ra' . Odd and even l -modes are presented separately in the first two cases due to the strong equatorial symmetry of the buoyancy force and the prominence of the $m = 8$ convective mode and $m = 0$ zonal mode leading to a dearth of odd- l buoyancy modes.

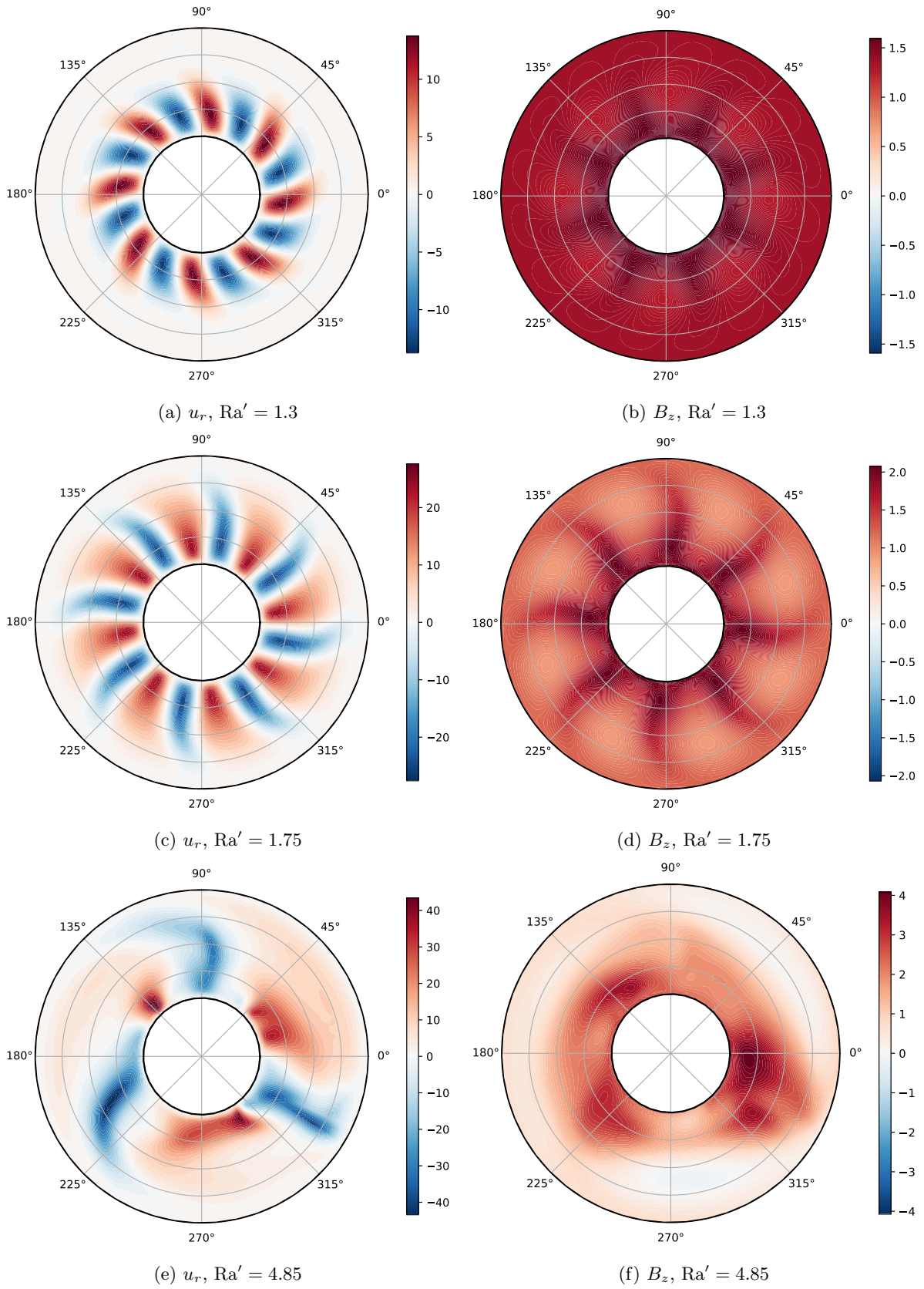


Figure 7: Equatorial sections for runs with $Pm = 1$ and $p_{10} = 1$. Longitudinal axes are included for comparison of the flow and field patterns.

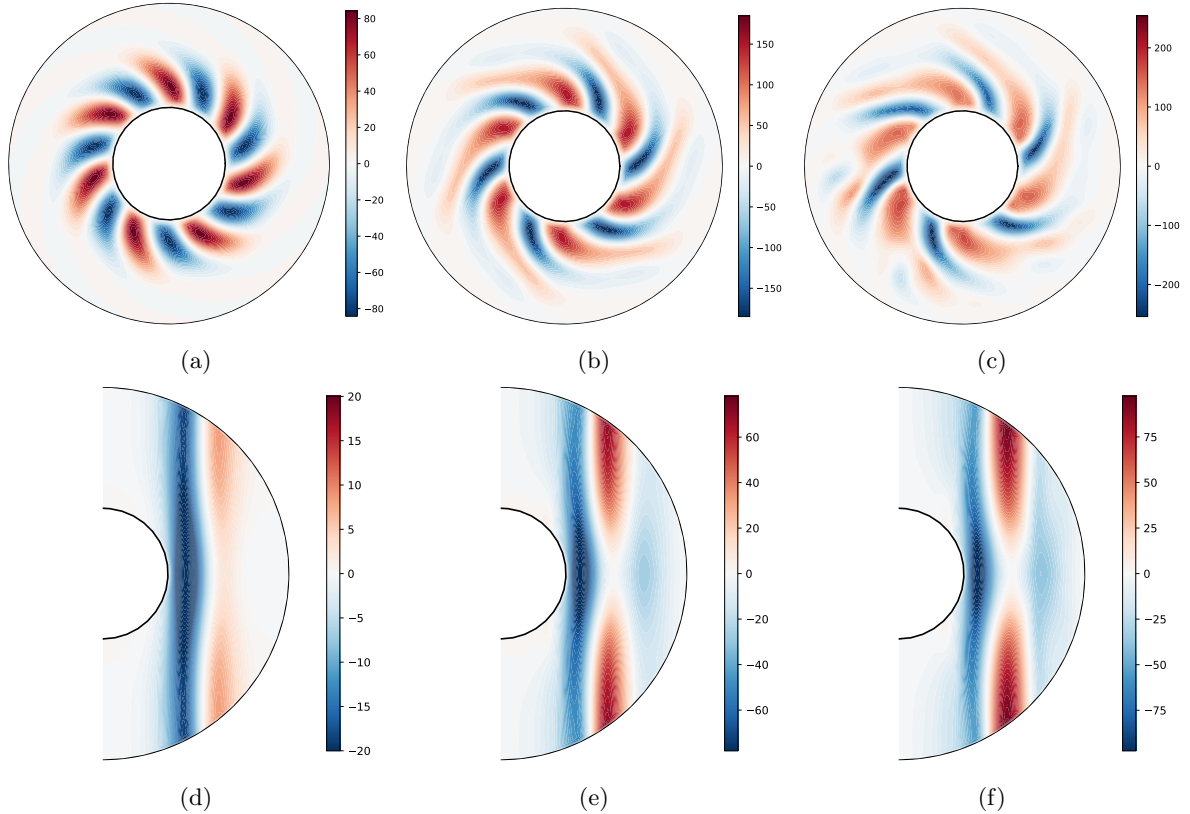


Figure 8: Equatorial sections of the radial velocity, $\hat{\mathbf{r}} \cdot \mathbf{u}$ (a-c), and zonal averages of the zonal velocity, $\hat{\phi} \cdot \mathbf{u}$ (d-f), in the columnar regime at $\text{Pm} = 5$ with $p_{10} = 0.1$ (cf. $\text{Pm} = 12$, Figure 12). a,d: $\text{Ra}' = 1.4$. b,e: $\text{Ra}' = 3.09$. c,f: $\text{Ra}' = 3.5$.

At slightly larger forcing, $\text{Ra}' = 1.75$, the flow strengthens and the axial field is further concentrated in the cold convective plumes (Figures 7c,d), which produces an asymmetry between the inward and outward flows. If we further increase the Rayleigh number then the $m = 8$ becomes unstable and successive lower-order modes are instead preferred. At $\text{Ra}' = 4.85$, the $m = 3$ mode is preferred, although the columns are unsteady, which spreads the axial field into a wider region (Figures 7e,f); these radial jets seem to correspond closely to the simulation presented by Sakuraba (2007), who instead finds a $m = 1$ mode to be preferred, as expected from magnetostrophic modes at smaller Ekman number (Sakuraba, 2002). This transition to non-axisymmetric inward and outward jets is also associated with a sharp increase in the toroidal magnetic field strength (Figure 5m) which additionally serves to promote the Lorentz force into the dominant balance at all scales (Figure 6, second row). At larger Ra' (Figure 6f, inertia and viscosity are pushed out of the dominant balance at all except the smallest length scales, leading to a clear MAC balance across scales.

In contrast to magnetoconvection, dynamo simulations at $\text{Pm} = 1$ do not generate magnetic fields of comparable large-scale strength over this Rayleigh number range, and therefore do not access the symmetry-breaking transition observed here for $p_{10} \sim 1$. This highlights the merit in using magnetoconvection models to isolate strong-field behaviour that would otherwise require substantially higher Ra' or Pm in fully self-consistent dynamo simulations.

4.2 Magnetoconvection with $\text{Pm} = 5$

At $\text{Pm} = 5$, magnetoconvection exhibits a wider set of flow regimes than at $\text{Pm} = 1$ since the magnetic field can grow larger as a result of the reduced dissipation. Over the range of Ra' , Pm , and p_{10} , we identify three distinct regimes as the imposed field strength is increased: (i) a weak-field columnar regime governed by a viscous–Archimedean–Coriolis (VAC) balance, (ii) an intermediate vacillating regime characterised by quasi-periodic growth and destruction of convective columns, and (iii) a strong-field regime dominated by radial jets and a magnetostrophic (MAC) balance; similar, but more pronounced than at $\text{Pm} = 1$. These regimes are most clearly distinguished by changes in columnarity, equatorial symmetry, and the

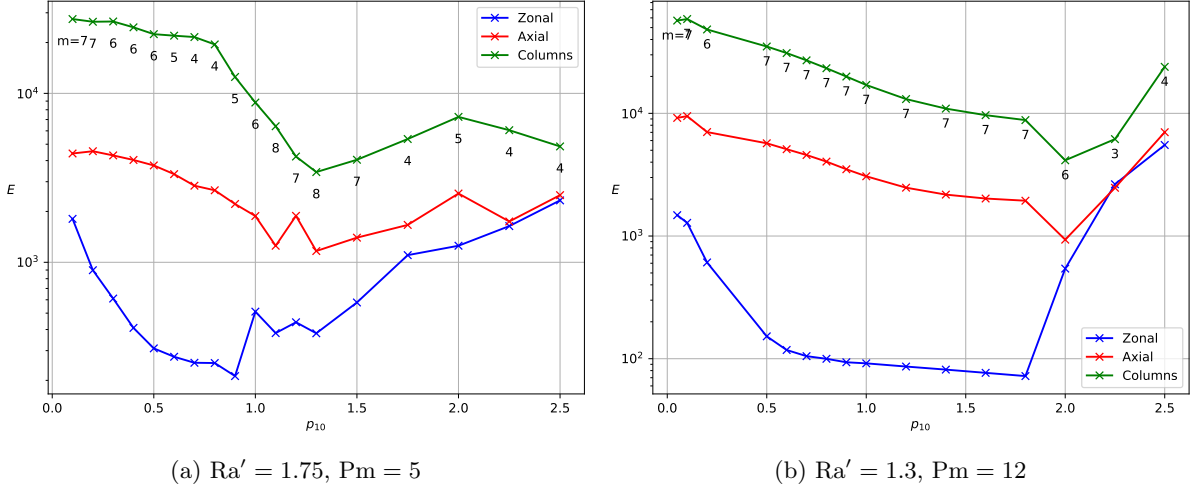


Figure 9: Kinetic energy of the three main components of columnar convection as p_{10} is varied. The dominant azimuthal mode is appended below the columnar energy curve.

partitioning of kinetic and magnetic energies shown in Figure 5. We discuss each regime in turn.

Weak-field columnar regime. For small imposed field strengths ($p_{10} \lesssim 0.8$, corresponding to $\Lambda \lesssim 1$), convection takes the form of geostrophic columns closely resembling the hydrodynamic solution and a leading-order VAC balance (Figure 10c shows that these simulations have a VAC balance for $l \geq 7$, with viscosity subdominant for l -modes below the order of the columnar mode). For $p_{10} = 0.1$, the geostrophic onset mode remains stable up to $Ra' \approx 3.5$, decreasing from $m = 7$ to $m = 6$ as Ra' increases. Figure 8 illustrates the evolution of the flow structure in this regime: as thermal forcing increases, the columns extend further radially and the preferred azimuthal wavenumber decreases, as in hydrodynamic rotating convection.

The zonal flow in this regime is weak and approximately z -independent at low Ra' , consistent with the hydrodynamic case (e.g. Simitev & Busse, 2003). As Ra' increases, the zonal flow strengthens and acquires a modest z -dependence, reflecting the increasing importance of the thermal wind. This behaviour is captured by the zonal component of the curl of the momentum equation (e.g. Aubert, 2005),

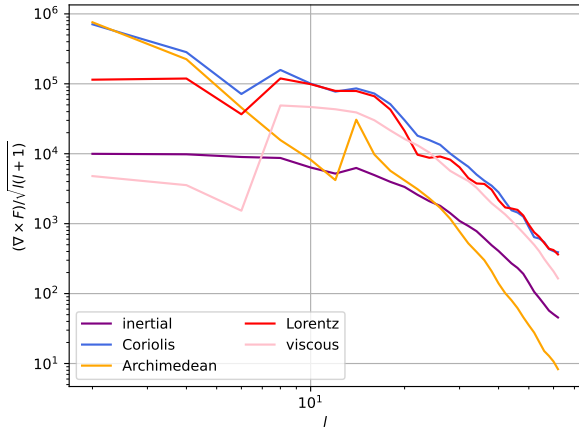
$$2 \frac{\partial u}{\partial \phi} = PmRa \frac{\partial [T]_{\phi}}{\partial \theta} + [\nabla \times (\mathbf{j} \times \mathbf{B})]_{\phi}, \quad (24)$$

where the Lorentz force contribution remains subdominant in this regime. The flow remains strongly equatorially symmetric and columnarity decreases only weakly with increasing Ra' (Figures 5e, 5b).

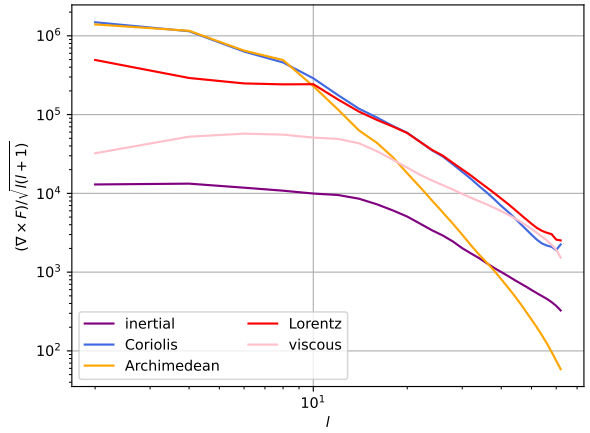
The relative contributions of the axial, columnar, and zonal components of the flow are shown in Figure 9a for simulations at fixed $Ra' = 1.75$ to highlight the effect of varying the magnetic field strength. As p_{10} increases within the weak-field regime, the dominant azimuthal mode decreases steadily from $m = 7$ to $m = 4$. The energies of the axial and columnar components decrease by approximately 25%, while the zonal flow energy is reduced by nearly an order of magnitude, indicating a suppression of large-scale zonal motion by the imposed magnetic field, with Ferraro's law of isorotation.

Intermediate vacillating regime. For intermediate imposed field strengths ($0.8 \lesssim p_{10} \lesssim 1.3$), the system enters a qualitatively different regime in which convective columns grow to moderate amplitude before becoming unstable and breaking apart in a quasi-periodic manner. Figure 11 captures a moment in this process for $p_{10} = 1.0$ and 1.2 at $Ra' = 1.75$. Columns initially grow at the horizontal scale of the linear mode and propagate azimuthally around the inner core. As they propagate, axial magnetic field is swept into the negative vorticity regions, leading to magnetic field amplification. Once sufficient magnetic flux is concentrated, the Lorentz force destabilises the column, causing it to break apart into smaller-scale turbulence. This turbulence disperses the magnetic field, and then diffuses itself, allowing the columnar structure to reform and the cycle repeats.

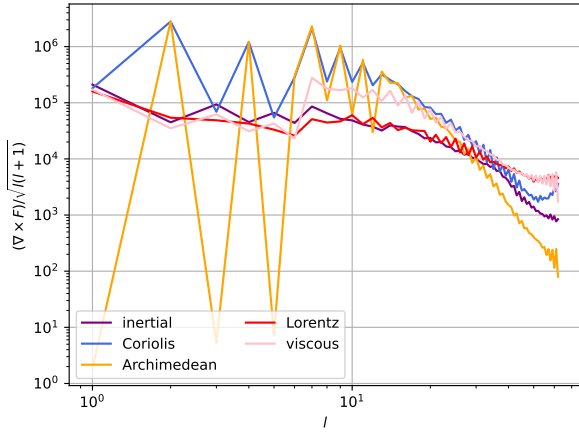
This vacillating behaviour is absent at smaller p_{10} , where the magnetic field is too weak to destabilise the columns, and at larger p_{10} , where a strong-field state can be maintained. It therefore represents a



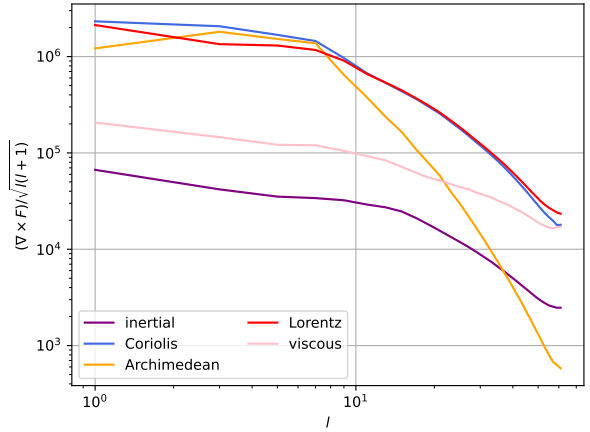
(a) $Ra' = 1.6, p_{10} = 1.0$



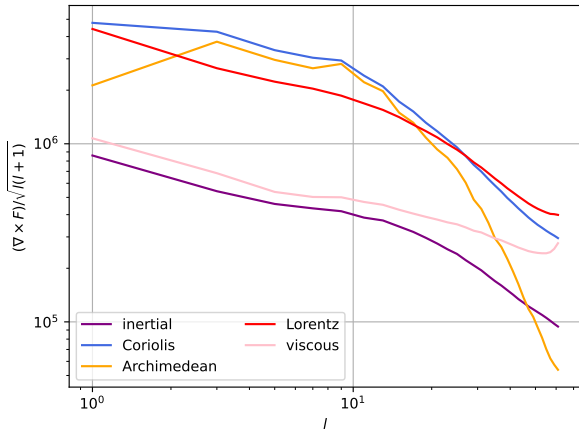
(b) $Ra' = 1.8, p_{10} = 1.0$



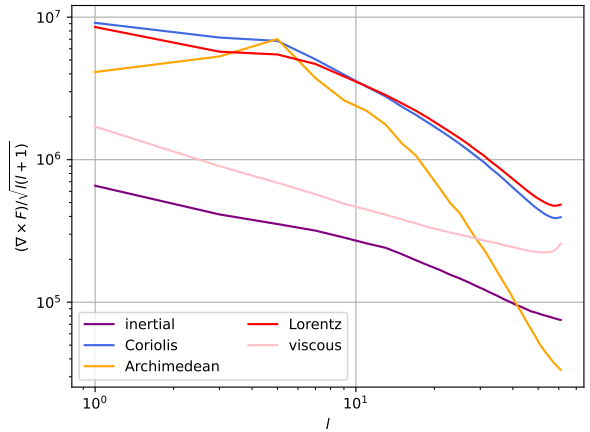
(c) $Ra' = 2.5, p_{10} = 0.1$



(d) $Ra' = 2.5, p_{10} = 1.0$



(e) $Ra' = 5.0, p_{10} = 0.1$



(f) $Ra' = 5.0, p_{10} = 1.0$

Figure 10: Time-averaged force spectra as in Figure 6, at $Pm = 5$, for $Ra' = 2.5$ and 5.0 for $p_{10} = 0.1$ and $Ra' = 1.6, 1.8, 2.5,$ and 5.0 for $p_{10} = 1.0$.

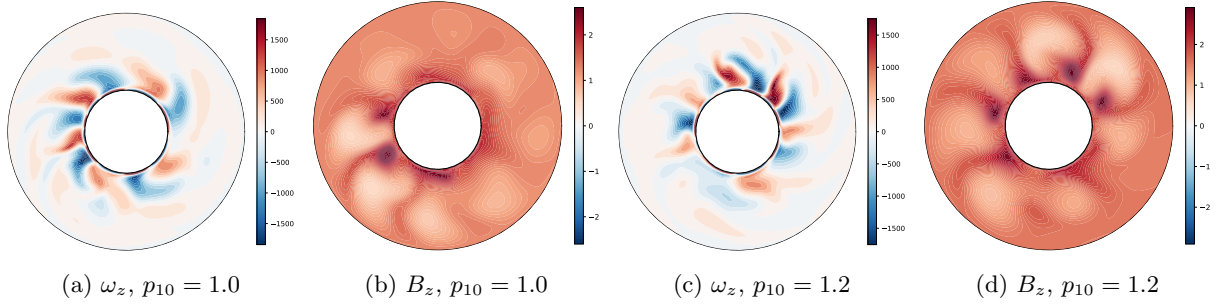


Figure 11: Contours of the axial vorticity and magnetic field strength at the equator at instants in simulations with $p_{10} = 1.0, 1.2$ with $Ra' = 1.75$ and $Pm = 5$ after a quasi-steady state has been reached. Note that, due to the symmetry of the flow, the vorticity and magnetic field have only a \hat{z} -component at the equator.

transitional regime between weak-field VAC dynamics and strong-field MAC dynamics. In the present simulations, quasi-periodic vacillations are observed for $p_{10} = 1.0$ over the range $1.7 \lesssim Ra' \lesssim 2.0$.

Figures 10a, 10b, and 10d show the force balances at $Ra' = 1.6, 1.8, 2.5$, below, within, and above the vacillating regime, respectively. In each case the force balance could be described as MAC, as the Lorentz force is consistently part of the dominant balance across a range of scales, however it is clear that there are subtle distinctions between the three cases. At $Ra' = 1.6$ and $Ra' = 1.8$, the Lorentz force does not enter the dominant balance at the largest scales, entering sharply at $l = 8$ for $Ra' = 1.6$, when the columns are steady, and gradually at $l \approx 10$, for $Ra' = 1.8$, when the columns are vacillating. The remaining forces are also smoother at $Ra' = 1.8$ than at $Ra' = 1.6$, consistent with the wide range of scales that emerge due to the break-up of the columns. Above the vacillating regime the Lorentz force also enters the dominant balance at smallest l , and viscosity and inertia are increasing subdominant.

Despite the strongly time-dependent nature of the vacillating flow, this regime remains largely equatorially symmetric (Figures 5e, 5h) and the columnarity decreases only gradually with increasing Ra' (Figure 5b), indicating that the instability is predominantly z -independent. The transition into this regime is, however, accompanied by a sharp increase in the toroidal magnetic energy (Figure 5n), reflecting enhanced field generation during the growth phase of the columns.

Strong-field regime. For sufficiently strong imposed fields ($p_{10} \gtrsim 1.3$, corresponding to $\Lambda \gtrsim 2$), columnar convection is replaced by large-scale radial jets similar to those observed at $Pm = 1$ and in previous studies of imposed-field magnetoconvection (Sakuraba, 2007). These jets are initially irregular close to the transition but become increasingly coherent and larger in scale as p_{10} is increased. Over this range, the dominant azimuthal mode decreases from $m = 8$ to $m = 4$, and the flow becomes strongly influenced by Lorentz forces at all but the smallest length scales.

In this regime, the zonal flow undergoes a marked increase in amplitude, approaching the strength of the axial and columnar components (Figure 9a). The structure of the zonal flow closely resembles that reported by Mason et al. (2022) for strongly imposed magnetic fields, in which the Lorentz force term in the zonal wind balance becomes dominant and directly drives large-scale zonal motion. Force spectra (Figure 10) confirm the emergence of a MAC balance across a wide range of spherical harmonic degrees, with inertia and viscosity confined to the smallest scales.

Equatorial symmetry breaking occurs for all values of p_{10} explored at sufficiently large Ra' (Figure 5e). This contrasts with the behaviour at $Pm = 1$ and highlights the increased susceptibility of higher- Pm flows to symmetry-breaking transitions under magnetic forcing. Equatorial symmetry breaking at $Pm = 5$ also correlates with a slight bump in the poloidal kinetic and magnetic energies (Figure 5k, 5n, unfilled diamonds) which would be consistent with symmetry-breaking corresponding to the onset of polar convective modes; however it would also be consistent with the development of a large scale meridional circulation. This relation emerges better at $Pm = 12$, where there is greater distinction between the two regimes.

For all values of p_{10} considered at $Pm = 5$, we observe a single continuous branch of magnetoconvective solutions with no evidence of bistability or hysteresis. While the vacillating regime provides a clear example of transitional dynamics between weak- and strong-field behaviour, its reliance on magnetic field

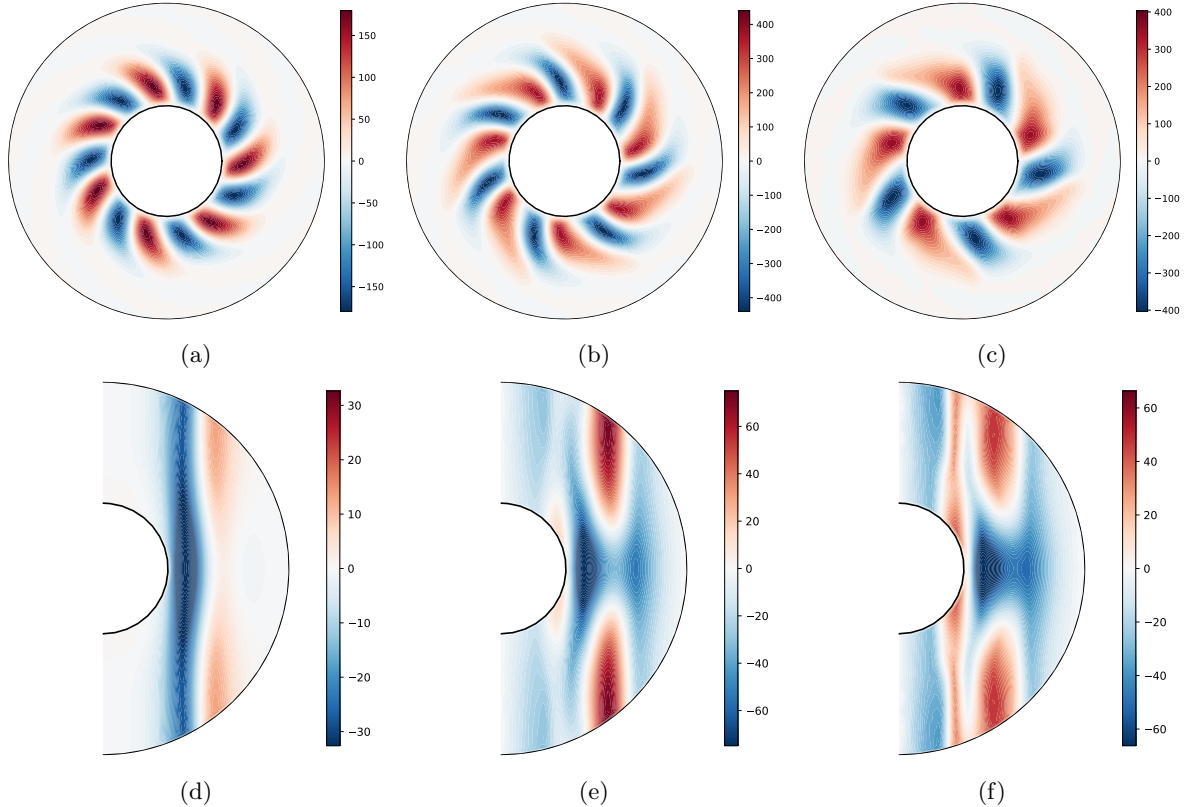


Figure 12: Equatorial sections of the radial velocity, $\hat{\mathbf{r}} \cdot \mathbf{u}$ (a-c), and zonally averaged plots of the zonal velocity, $\hat{\phi} \cdot \mathbf{u}$ (d-f), at a quasi-steady instant in two simulations in the columnar regime of convection, close to onset, with $p_{10} = 0.1$ and $\text{Pm} = 12$. (a,d): $\text{Ra}' = 1.3$. (b,e): $\text{Ra}' = 2.4$ (pre-mode change). (c,f): $\text{Ra}' = 2.4$ (post-mode change).

concentration at scales smaller than the convection columns suggests that it is unlikely to persist at very small magnetic Prandtl numbers, such as those relevant to planetary cores.

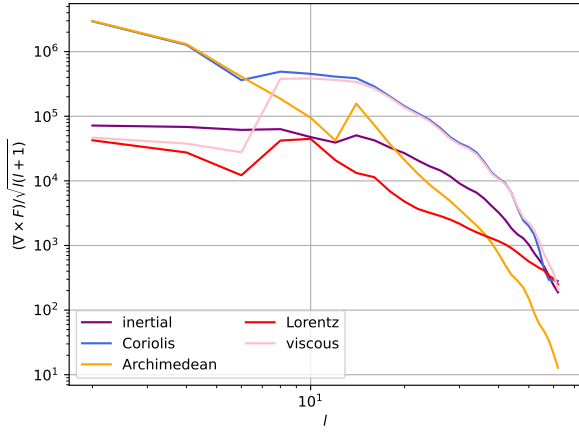
4.3 Magnetoconvection with $\text{Pm} = 12$

At $\text{Pm} = 12$, magnetoconvection exhibits the same broad sequence of regimes as at $\text{Pm} = 5$, but with several key differences that stem from the reduced magnetic diffusivity. In particular, the weaker diffusion permits more complex magnetic field structures and sharper distinctions between weak-field, transitional, and strong-field behaviour. This parameter regime is of particular interest because dynamo simulations at comparable Pm exhibit the widest region of bistability so far observed between weak- and strong-field branches.

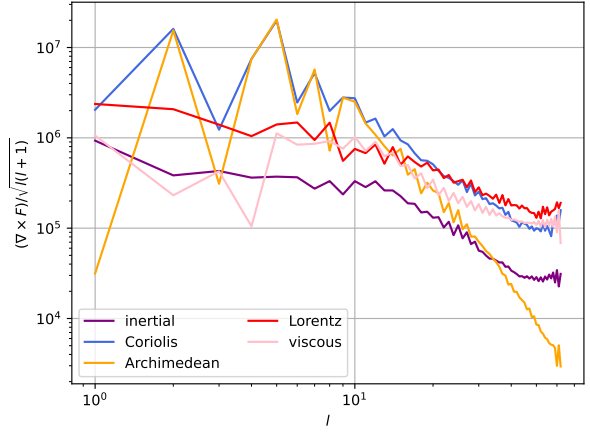
Weak-field regime. We first consider weak imposed field simulations with $p_{10} = 0.1$. Figure 12a shows a representative case at weakly supercritical Rayleigh number, for which the flow structure is a small perturbation of the hydrodynamic solution; this is consistent with the force spectra (Figure 13a) which show that the Lorentz force remains subdominant to the Coriolis, viscous, and inertial forces at all length scales. The poloidal magnetic field is largely axial and closely resembles the imposed background field, while an induced toroidal field is generated, predominantly outside the tangent cylinder (Figures 14a, 14b).

As the Rayleigh number is increased, the columnar convection strengthens and expands radially, while the development of an equatorial thermal anomaly modifies the zonal flow profile (Figures 12b, 12e), in a manner analogous to lower Pm cases. At the same time, the mean poloidal magnetic field transitions from an axial to a dipolar configuration (Figure 14c), and the induced toroidal field extends into the tangent cylinder (Figure 14d). This state becomes marginally unstable at $\text{Ra}' \approx 2.4$ and persists for only a fraction of a magnetic diffusion time before reorganising into an $m = 5$ convective mode (Figure 15).

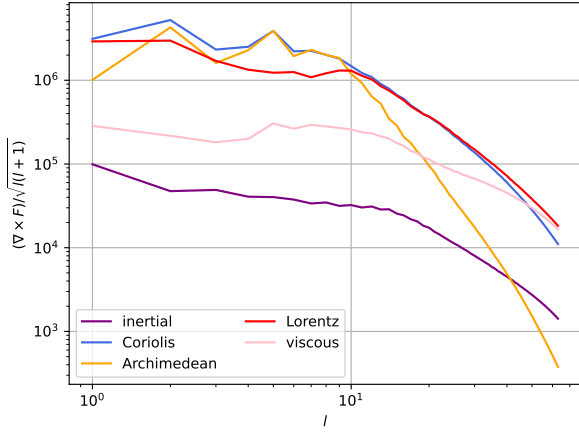
Figure 14e shows that this mode transition is accompanied by a substantial increase in the strength of the



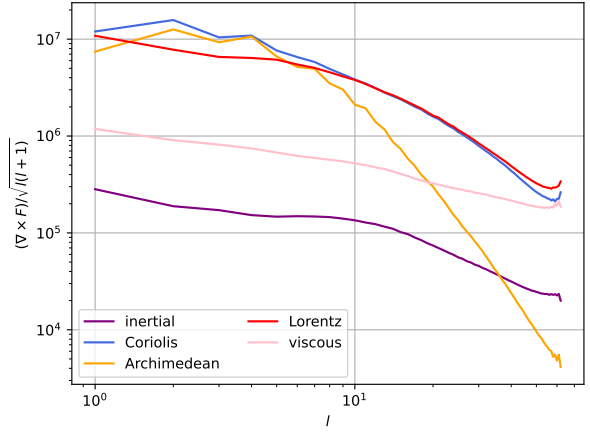
(a) $Ra' = 1.3$, $p_{10} = 0.1$ (even modes only).



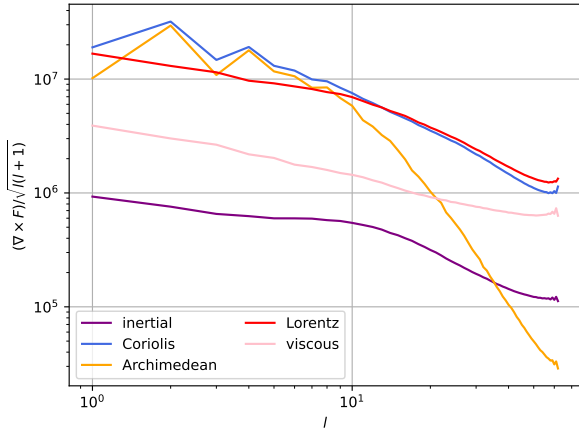
(b) $Ra' = 2.4$, $p_{10} = 0.1$ (weak-field, $m = 5$ mode).



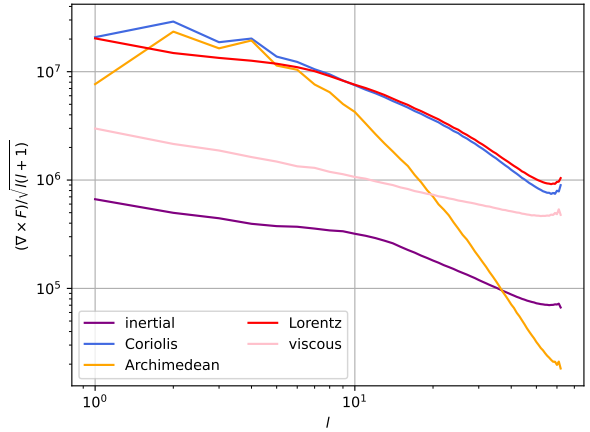
(c) $Ra' = 1.6$, $p_{10} = 1.0$.



(d) $Ra' = 2.0$, $p_{10} = 1.0$.



(e) $Ra' = 2.4$, $p_{10} = 0.1$ (strong-field).



(f) $Ra' = 2.4$, $p_{10} = 1.0$.

Figure 13: Force spectra as in Figure 6 at $Pm = 12$. Top row: weak-field. Middle: vacillating. Bottom: Strong-field.

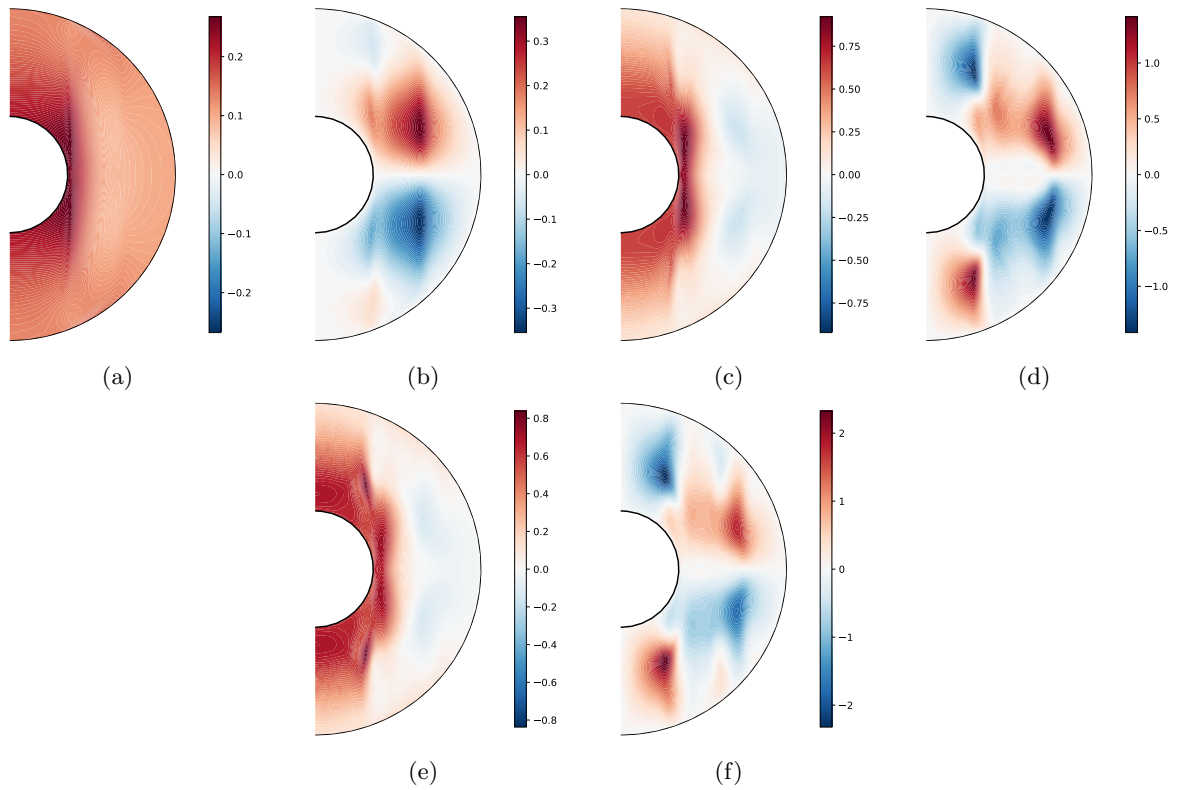


Figure 14: Meridional sections of the zonally averaged vertical, \hat{z} (a,c,e), and zonal, $\hat{\phi}$ (b,d,f), components of the magnetic field in the weak-field regime. $Ra' = 1.3$, $Pm = 12$, and $p_{10} = 0.1$ (a,b) and $Ra' = 2.4$, $Pm = 12$, and $p_{10} = 0.1$ pre-mode change (c,d) and post (e,f).

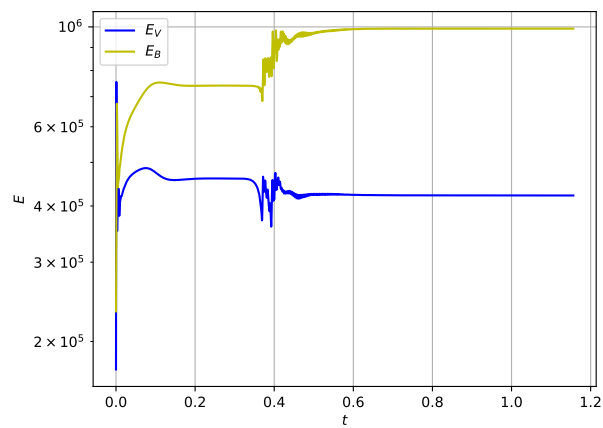


Figure 15: Kinetic and magnetic energies over time of the simulation with $p_{10} = 0.1$, $Ra' = 2.4$, corresponding to the centre and right plots of Figure 12.

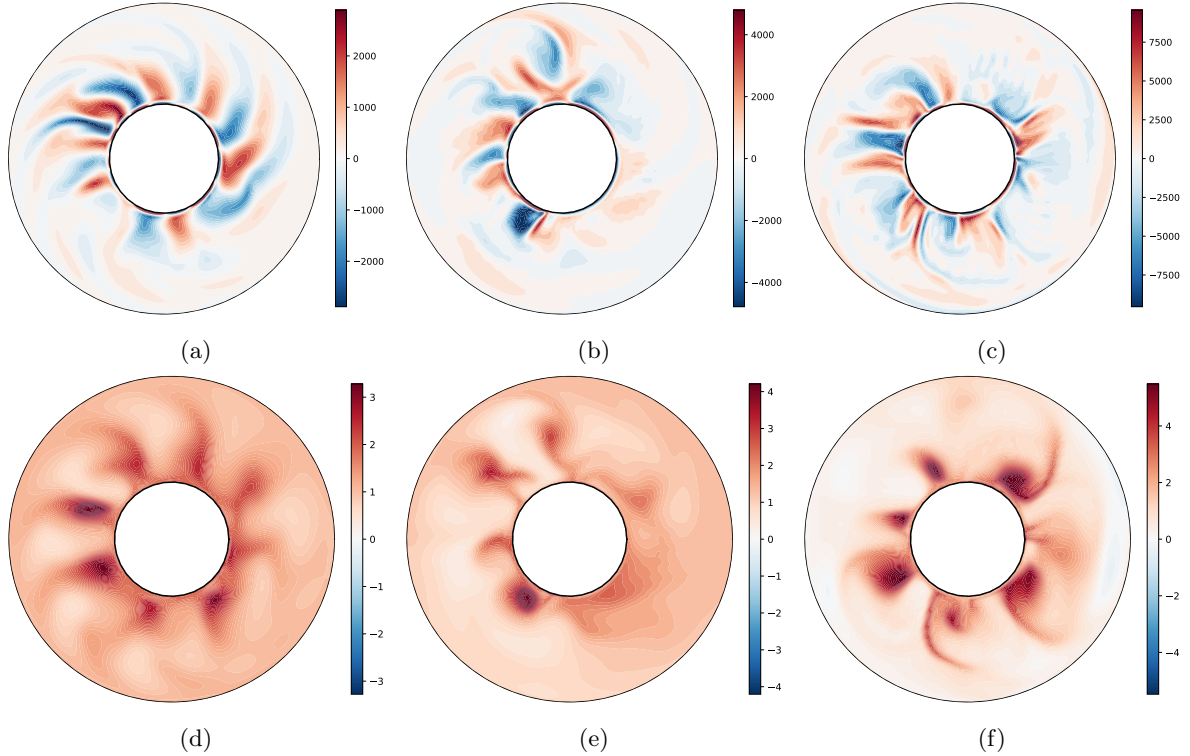


Figure 16: Equatorial sections of the axial vorticity, $\hat{\mathbf{z}} \cdot \boldsymbol{\omega}$ (a-c), and the axial magnetic field, $\hat{\mathbf{z}} \cdot \mathbf{B}$ (d-f), at a quasi-steady instant in three simulations in the vacillating \rightarrow strong-field regime, with $p_{10} = 1.0$. (a,d): $\text{Ra}' = 1.6$. (b,e): $\text{Ra}' = 1.75$. (c,f): $\text{Ra}' = 2.0$.

toroidal magnetic field. This increase can be interpreted as arising from an effective increase in the magnetic Reynolds number, $\text{Rm} = U\ell/\eta$, driven primarily by the increase in the dominant horizontal length scale ℓ , while the overall structure of the flow remains largely unchanged. It is plausible that a sequence of similar transitions, progressively increasing the convective length scale and magnetic field strength, could ultimately lead to the collapse of the weak-field branch. Notably, the instability at $\text{Ra}' \approx 2.4$ occurs just above the collapse of the weak-field branch in dynamo simulations at comparable parameters ($\text{Ra}' \approx 2.38$, Teed & Dormy, 2025a), suggesting that the large-scale field is not solely responsible for inciting the collapse of the weak-field branch, and that the alternative boundary condition restriction in our magnetoconvection models that poloidal modes with $(l, m) > (1, 0)$ must vanish at the outer boundary can delay, but not suppress, it.

Despite the apparently simple flow structure in this regime, the force spectra (Figure 13b) reveal a complex balance: all five forces contribute at comparable orders across much of the spectrum, though inertia is consistently weak. The key distinction between this weak-field state and strong-field states is that the viscous force continues to compete with the Lorentz force at several length scales, preventing the establishment of a clear MAC balance. This hierarchy, where both Lorentz and viscous forces are important across a range of scales, is reminiscent of a ‘VMAC’ balance observed in weak-field non-dipolar dynamo simulations (Teed & Dormy, 2025b).

Vacillating regime. For intermediate imposed field strengths, most clearly illustrated at $p_{10} = 1.0$, the weak-field regime transitions through a vacillating state before reaching strong-field behaviour. Figure 16 illustrates this regime, showing the close correspondence between regions of intense negative axial vorticity and concentrations of strong axial magnetic field. At smaller Rayleigh numbers, these regions of condensed magnetic field form and disperse regularly as the amplified field destabilises the convection columns. As Ra' increases, the magnetic field amplification becomes sufficiently strong to modify the convective structures themselves, producing longer-lived (but more chaotic) structures.

Compared with the corresponding vacillating regime at $\text{Pm} = 5$ (Figure 11), the magnetic field at $\text{Pm} = 12$ is amplified to significantly greater strengths relative to the imposed background field, reflecting the reduced magnetic diffusion. In force spectra, the distinction between vacillating and fully strong-field

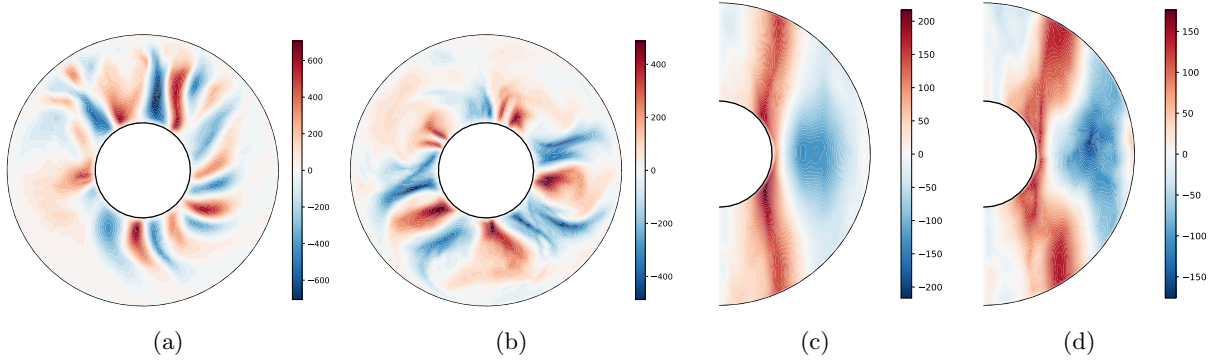


Figure 17: Equatorial sections of the radial velocity, $\hat{r} \cdot \mathbf{u}$ (a,b), and zonally averaged plots of the zonal velocity, $\hat{\phi} \cdot \mathbf{u}$ (c,d), at a quasi-steady instant in two simulations in the strong (MAC) regime, with $Ra' = 2.65$. (a,c): $p_{10} = 0.1$. (b,d): $p_{10} = 1.0$.

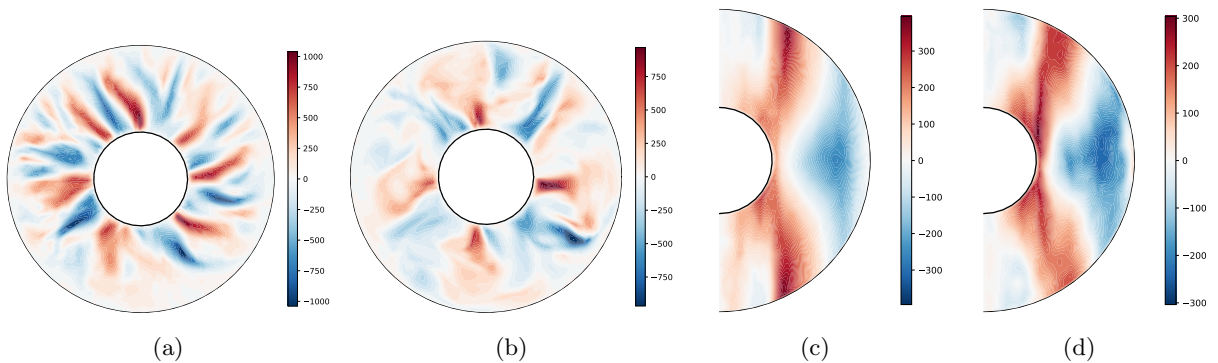


Figure 18: As in Figure 17 with stronger forcing, $Ra' = 4.0$.

states is most clearly observed through the viscous force. At $Ra' = 1.6$ for $Pm = 12$ (Figure 13c) and $Ra' = 1.8$ for $Pm = 5$ (Figure 10b), the viscous force exhibits a modest enhancement at the harmonic order corresponding to that of the vacillating columns. This feature is much smoother than in the weak-field regime (e.g. Figure 13b), reflecting the broader range of scales that emerge as a result of the break-down of the columns.

As Ra' increases further, the vacillating regime transitions smoothly to the strong-field regime. Distinguishing these two regimes on the basis of force spectra alone becomes increasingly difficult between $Ra' \approx 2.0$ and 2.4 , although the equatorial symmetry of the flow differs between these cases.

Strong-field regime. For $p_{10} = 1.0$, equatorial symmetry is broken at $Ra' \approx 2.4$; however, this symmetry breaking has little immediate impact on either the force spectra or the overall structure of the flow. At Rayleigh numbers $Ra' \gtrsim 2.4$, both the compensated-curl force spectra (Figure 13f) and the flow morphology (Figures 17, 18) closely resemble those observed in strong-field dynamo simulations at comparable parameters (see §3.2; Teed & Dormy, 2023). Rather than a sharp transition as observed in dynamo simulations, the emergence of strong-field behaviour therefore occurs gradually over the range $1.6 \lesssim Ra' \lesssim 2.0$.

In contrast, for weaker imposed fields ($p_{10} = 0.1$), the transition to strong-field behaviour is abrupt and coincides with the breaking of equatorial symmetry. This sharp transition is associated with the sudden excitation of a new set of modes (Guseva et al., 2025), which significantly enhances the strength of the poloidal flow (Figure 5l) and hence the poloidal magnetic field (Figure 5o). This increase in magnetic field strength then allows the flow to reorganise into a structure closely resembling that found in the strong imposed field simulations at $p_{10} = 1.0$.

Figure 19a shows the zonally averaged poloidal streamlines for a weak-field solution at a bistable point in parameter space. The streamlines are equatorially symmetric and primarily reflect the axial circulation within convection columns, with neighbouring counter-rotating cells persisting after zonal averaging due to slight asymmetries between cyclonic and anti-cyclonic columns. On the strong-field branch, the

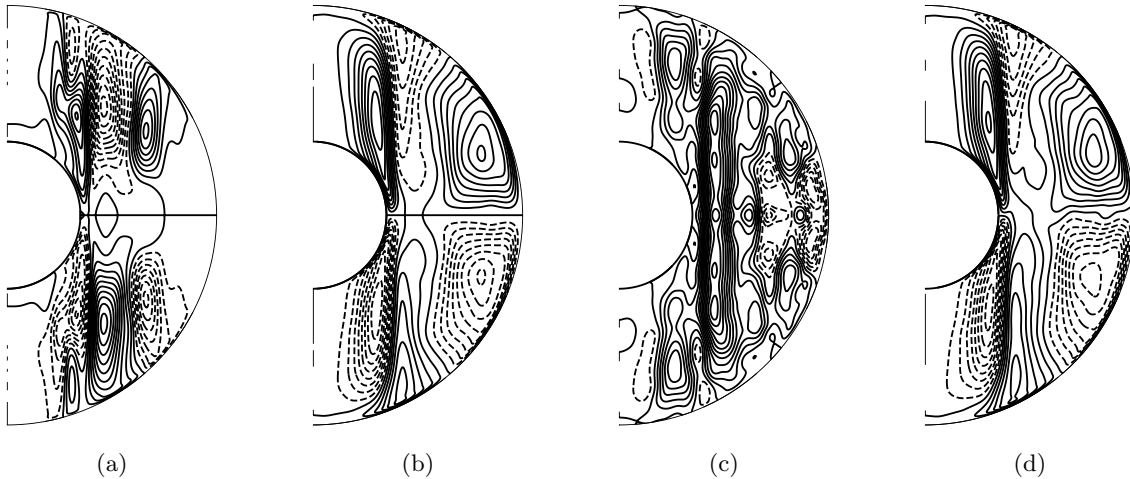


Figure 19: Streamlines of the temporally- and zonally-averaged poloidal flow, $Ra' = 2.4$, $Pm = 12$, $p_{10} = 0.1$. (a) The weak-field (equatorially symmetric) branch (b)-(d) The strong-field branch, displayed as the streamlines of the equatorially symmetric and antisymmetric, and total flow, respectively. Solid streamlines represent clockwise-rotating flow, and dashed streamlines, anti-clockwise.

zonally averaged streamlines remain largely equatorially symmetric (Figure 19d), consistent with $s_u > 0$ (Figure 5f), but the circulation cells extend much further into the equatorial region and inside the tangent cylinder. This reflects the increased magnetic field strength, which allows the Lorentz force to overcome the rotational constraint in regions where the boundaries are closest and (hence) the Coriolis force is most strongly felt.

By decomposing the flow into its symmetric and antisymmetric components (Figures 19b, 19c), we also identify the development of a meridional circulation aligned with a cylindrical surface at approximately half the outer radius. This circulation separates the two dominant symmetric circulation cells and may provide support for the maintenance of a large-scale magnetic field in the strong-field regime.

5 Conclusions

In §3.2 we find that the weak-strong transition in dynamo simulations leads to a spontaneous breaking of the equatorial symmetry of the weak-field, highly-columnar, state, as the Rayleigh number is increased. There are three plausible candidates for the onset mechanism of the antisymmetric modes:

- (i) That convection rolls break apart due to an inertial instability.
- (ii) That convection rolls break apart due to a magnetic instability.
- (iii) That a new instability occurs, possibly triggered by, but evolving independently of, the existing convection rolls.

Case (i) seems plausible since the inertia of convection rolls increases with the Rayleigh number. At sufficiently large Ra columnar flow can then become unstable to a buckling instability (like the Billant instability), which could lead to the emergence of modes antisymmetric about the equator. This hypothesis, however, is not supported by §3.1, and Figures 1a,1b, in particular, which show that the columnarity of the flow (in the bulk of the shell) is reduced at lower Rayleigh numbers than the occurrence of symmetry-breaking, which occurs at $Ra' \approx 10$. By this point the columnarity of the flow has fallen to around 0.6, which is significantly smaller than in some (weakly supercritical) strong-field states (Figures 4a,4b). Though this instability may be responsible for an alternative transition (at these large Ra) to inertially-driven/inertially-influenced states that may correspond/be relevant to multipolar solutions commonly found in dynamo simulations.

Case (ii) contends instead that equatorial symmetry-breaking occurs due to the onset of a magnetically-induced instability of the convection rolls. In magnetoconvection simulations, particularly at high $Pm \gtrsim 5$ and magnetic field strength $p_{10} \gtrsim 1.0$, we find evidence that such an instability occurs, although we also find that it is not clearly correlated with symmetry-breaking.

This magnetic instability may be equivalent to that found by Sakuraba (2007). It is well-known that columnar convection is more efficient at transporting heat at the equator since the convection roll is closer there to the inner core; this produces a temperature anomaly at the equator which drives a flow away from (towards) the equator in (anti)cyclonic vortices (Jones, 2011). Incompressibility of the flow then requires that flow is drawn, at the equator, into cyclonic rolls, which leads to a destabilising accumulation of magnetic field lines in those rolls. Since this process takes a finite amount of time, the progressive formation and destabilisation of rolls can be observed in some magnetoconvection simulations. Although this process does not produce equatorial symmetry-breaking, it may be an important mechanism in disrupting columnar flow in the fluid bulk as the magnetic field strength is increased. Force spectra in these vacillating simulations are very similar to force spectra in strong-field simulations.

The effectiveness of this instability mechanism will be dependent on the horizontal length scale of the columns, the strength of the axial flow through the columns, and most critically on the rate of magnetic diffusion; hence it will depend on all model parameters. Since spherical simulations modelling magnetohydrodynamic processes relevant to astrophysical bodies (including those reported here) are generally performed at far larger Pm than expected for natural dynamos (such as the geodynamo), the effectiveness of this mechanism may be over-enhanced in simulation compared to reality.

By contradiction, therefore, we are left with case (iii): that equatorial symmetry-breaking occurs due to an instability that does not involve convection rolls.

Gilman (1975) and Sreenivasan & Jones (2006) have previously considered the consequences of the onset of convection inside the tangent cylinder, which can be well-approximated by the linear instability of a magnetic conduction state due to the relative quiescence of the tangent cylinder as a result the enhanced constraint of rapid rotation due to the closeness, in z , of the inner and outer boundaries. The Lorentz force, in rapidly-rotating magnetoconvection, can overcome the Taylor-Proudman constraint at significantly lower Rayleigh numbers than the viscous force alone (Fearn, 1979). Sreenivasan & Jones (2006) find that an axial magnetic field reduces the critical Rayleigh number by around a factor of three, and the further addition of a strong toroidal magnetic field, which is also present in the tangent cylinder in models of weak-field convection (Figure 14), would only compound this effect. At $\text{Pm} = 5$, symmetry-breaking can occur at around $\text{Ra}' = 3.3$, (three times less than in purely hydrodynamic simulations where the symmetry-breaking must wait for inertial effects), whilst at $\text{Pm} = 12$, this occurs at $\text{Ra}' = 2$.

Appendix B outlines a possible reasoning for polar convection to appear preferentially as an antisymmetric, rather than a symmetric mode, despite the disconnection of the regions within the tangent cylinder above and below the inner core. Hence, it seems that by measuring the departure of the flow from equatorial symmetry, we do indeed capture the onset of polar convection.

Untangling the cause and effect in the correlation between the onset of polar convection and the onset of the strong-field regime is challenging and could be an interesting subject for future work. Skene et al. (2024) investigate the case of bistability between a hydrodynamic and a weak-field state using an adjoint method, and hence are able to determine an unstable fixed point that influences the evolution of an initial state towards either a successful or failed dynamo. If similar methods can be employed between the weak- and strong-field branches it may help to understand the exact role that the onset of polar convection has in the development of the strong-field regime.

There is also a clear mechanism by which polar convection directly supports the poloidal magnetic field. Polar convection generally onsets as a thin, rising and falling plumes in which the z -vorticity changes sign at the top and bottom of each plume (Chandrasekhar, 1961; Sreenivasan & Jones, 2006); this provides a direct source of poloidal flow from which a poloidal field can be amplified from a toroidal one. This is consistent with our observations; Figure 5 shows that the poloidal kinetic energy consistently jumps with the onset of strong-field convection, which could also be explained by the stronger magnetic field supporting the flow in overcoming the rotational constraint. However, the same results also show that increasing the strength of the imposed field reduces both components of the kinetic energy. The stronger poloidal flow can also be seen to reduce the ratio between the energies in the toroidal and poloidal magnetic fields.

An analysis of the linear problem, including a tracking of individual onset modes, was performed by Sakuraba (2002). However, further consideration of the linear problem may be useful to isolate the onset of the polar convective modes and the effect of variation of the magnetic Prandtl number. Accurately determining the critical Rayleigh number for the onset of polar (magneto)convection in a spherical shell may enable prediction of the onset of the strong-field branch and suggest regions of bistability in dynamo

simulations, without the need to perform suites of costly simulations.

In this paper, we use magnetoconvection simulations to examine a transition between weak- and strong-field solutions reminiscent of those found in dynamo simulations (Dormy, 2016; Teed & Dormy, 2025a). Two further transitions are important in understanding the solution space of (Boussinesq, spherical-shell) dynamo simulations: these are the transition between regimes with multipolar and strong-field dipolar magnetic fields, and the transition from $\text{Pm} > 1$ to $\text{Pm} \ll 1$, which is important for correctly capturing the effect of small-scale turbulence in models (Tobias, 2021). These two problems can both be better understood making use of magnetoconvection simulations, and will be the subject of future work.

A Magnetic boundary conditions

A.1 Electrically-conducting boundaries

To a reasonable approximation, the Earth's mantle is electrically insulating. In an insulating medium,

$$\mathbf{j} = \mathbf{0}. \quad (25)$$

Decomposed into poloidal and toroidal components, \mathbf{B} and \mathbf{j} are

$$\mathbf{B} = \nabla \times \nabla \times (B_p \mathbf{r}) + \nabla \times (B_t \mathbf{r}), \quad (26a)$$

$$\mathbf{j} = \nabla \times \nabla \times (j_p \mathbf{r}) + \nabla \times (j_t \mathbf{r}). \quad (26b)$$

Which, by definition, are related by

$$j_p = B_t, \quad j_t = -\nabla^2 B_p, \quad (27)$$

hence, the magnetic field in an insulating medium must satisfy the

$$B_t = \nabla^2 B_p = 0. \quad (28)$$

Given that B_p, B_t , can be decomposed into spherical harmonics as

$$B_p = \sum_l \sum_m P_l^m(r) Y_l^m(\theta, \phi), \quad B_t = \sum_l \sum_m T_l^m(r) Y_l^m(\theta, \phi) \quad (29)$$

then

$$T_l^m = 0, \quad (30a)$$

$$\left[r^2 \frac{d^2}{dr^2} + 2r \frac{d}{dr} - l(l+1) \right] P_l^m = 0, \quad (30b)$$

for all l, m . Equation (30b) admits solutions $P_l^m \sim r^\alpha$ with α satisfying $\alpha(\alpha+1) = l(l+1)$ which has particular solutions $\alpha = l$ (corresponding to external sources, since $l > 0$) and $\alpha = -l-1$ (corresponding to internal sources).

If there are no external sources then the exterior magnetic field is $P_l^m = Ar^{-l-1}$, for some constant A , and so the boundary condition on the internal field, matching with this solution is

$$\left(r \frac{d}{dr} + l(l+1) \right) P_l^m \Big|_{r=r_o} = 0, \quad \forall l, m. \quad (31)$$

At the inner boundary the role of internal and external sources are reversed by the geometry in relation to increasing r , i.e., sources correspond to $\alpha = l$, hence, the condition at the inner boundary is

$$\left(r \frac{d}{dr} - l \right) P_l^m \Big|_{r=r_I} = 0, \quad \forall l, m. \quad (32)$$

Say an external source exists which induces a uniform axial magnetic field of the form $\mathbf{B} = B_0 \hat{\mathbf{z}}$ where $\hat{\mathbf{z}} = \cos \theta \hat{\mathbf{r}} - \sin \theta \hat{\boldsymbol{\theta}}$. Then, given $B_r = r^{-1} L^2 B_p$ (where $L^2 = l(l+1)$), this axial field takes the form

$$B_p(r, \theta, \phi) = P_1^0(r) \sqrt{3} \cos \theta, \quad P_1^0(r) = \frac{B_0}{2\sqrt{3}} r. \quad (33)$$

The exterior magnetic field is then a compound of the internal and external sources, i.e.,

$$P_1^0 = \frac{B_0}{2\sqrt{3}}r + \frac{A_1^0}{r^2}, \quad P_l^m = A_l^m r^{-l-1}, \quad (l, m) \neq (1, 0), \quad (34)$$

with A_l^m arbitrary constants. This implies that the boundary conditions on the $(1, 0)$ mode are modified to

$$\left(\frac{d}{dr} + \frac{2}{r} \right) B_P \Big|_{r=r_o, (l,m)=(1,0)} = \frac{\sqrt{3}B_0}{2}, \quad (35)$$

whilst the boundary conditions on all other modes remain the same.

A.2 Perfectly-conducting boundaries

In magnetoconvection problems, an external magnetic field is applied to the system, that is, we can write

$$\mathbf{B} = \mathbf{B}_0 + \mathbf{B}', \quad (36)$$

where \mathbf{B}_0 is a fixed, known field, and \mathbf{B}' is induced by the motion of the fluid. Here, as in many other studies, we assume that the imposed field is axial and uniform, i.e.,

$$\mathbf{B}_0 = B_0 \hat{\mathbf{z}}. \quad (37)$$

One option now is to assume that the varying field, \mathbf{B}' , is insulating

Another option is to fix the magnetic field at the outer boundary. By this we mean that $B_P(r_o, l, m)$ is fixed for all l, m (generally, $B_P(r_o, l, m) = 0$ for all $(l, m) \neq (1, 0)$). Immediately, this is different to (31) and (34), since this condition applies directly to B_P rather than its derivative.

In the GSD code, say we set $P_1^0(r_o) = C$. The radial component of the magnetic field is given by

$$B_r(r, \theta, \phi) = \sum_{l,m} l(l+1) \frac{P_l^m(r)}{r} \cdot \hat{Y}_l^m(\theta, \phi) \quad (38)$$

and hence, setting all $P_l^m = 0$, $(l, m) \neq (1, 0)$,

$$B_r(r_o, \theta, \phi) = 2 \frac{C}{r_o} \left[\frac{1}{2} \frac{d}{d\mu} (\mu^2 - 1) \right]_{\mu=\cos\theta} = \frac{2C}{r_o} \cos\theta = \frac{13C}{10} \cos\theta, \quad (39)$$

where $r_o = 20/13$. This can be easily verified. Furthermore, the appropriate scale factor between the external field, B_0 , and the fixed poloidal, C , boundary conditions is $2/r_o$.

B Equatorial symmetry

In this appendix, we explain the origin of the terms *equatorial* and *polar* symmetry and their connection with the odd and even modes of (magneto)convection (sometimes called modes with Roberts/Busse symmetry) that are reported by many authors (e.g. Fearn, 1979; Sakuraba, 2002; Seeley et al., 2025).

Full sphere Roberts (1968) derived the equations governing the onset of hydrodynamic convection in a sphere via internal heat sources; he noted that, after considering solutions in the form of spherical harmonics, the structure of the resultant equations leads to two distinct families of solutions emerging, which are characterised by the parity of $l + m$, where l, m are the spherical harmonic degree and order, respectively, of U and T , where

$$\mathbf{u} = \nabla \times \nabla \times U \mathbf{r} + \nabla \times V \mathbf{r}. \quad (40)$$

The coupled harmonics of V have opposite parity. Hence, it can be seen that for even modes (modes with $l + m$ of U , even) u_r , u_ϕ , and T will be symmetric about the equator, whilst u_θ , u_z will be antisymmetric, corresponding to a mirror symmetry of \mathbf{u} about the equator. Similarly, odd modes correspond with mirror-antisymmetry about the equator.

In the axisymmetric, $m = 0$, case, Roberts (1968) shows that the odd modes are the most unstable - this solution corresponds to a global meridional circulation, with streamlines corresponding to hemispherical

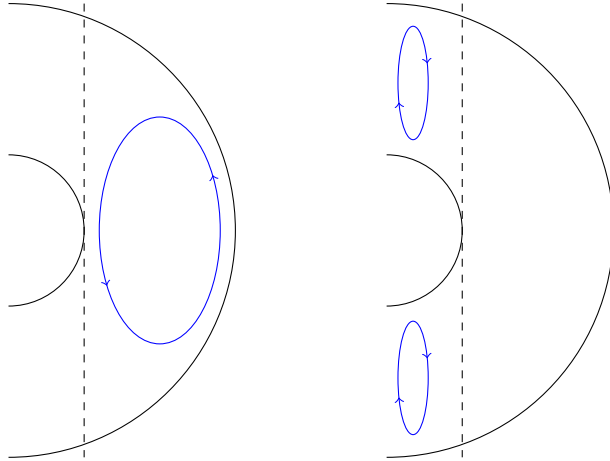


Figure 20: Streamlines of (a) Meridional convection outside the tangent cylinder. (b) Meridional convection inside the tangent cylinder.

rings. Roberts similarly calculates the critical Rayleigh numbers for odd modes with $m > 0$. For this reason, odd modes can be referred to as Roberts symmetry.

Busse (1970) then tackles a perturbation analysis for the spherical convection problem and calculates the critical Rayleigh numbers of the even modes, showing that these are preferred at onset for $m > 0$ and generally preferred when considering all m , for small Ekman numbers. These modes include tall thin columnar structures appearing at onset as thermal Rossby waves. This symmetry is sometimes called Busse symmetry and is frequently taken as an assumption in linear onset convection studies to simplify the analysis.

Meridional convection is efficient at transporting heat since a significant portion of the velocity is directed in the radial direction; however, the gradients of the velocity parallel to the rotation axis will also be large, so at onset the flow must contest with the stabilising effect of the Taylor-Proudman constraint. Thermal Rossby waves are less efficient at transporting heat since the flow is only partly radial, except at the equator; however, they can almost take the form of perfect Taylor columns, with only small perturbations required at the outer boundaries. Hence, for sufficiently small Ekman numbers, it is safe to expect that the Busse modes will have a smaller critical Rayleigh number.

Effect of an inner core If an inner core is present, global meridional convection becomes impossible, and large scale meridional convection must be restricted to the outside of the tangent cylinder (Figure 20a). Smaller convection cells could also develop inside the tangent cylinder (Figure 20b); these latter modes can be efficient in transporting heat, since streamlines abut both the inner and outer boundaries, however, they are impeded by viscosity due to their small scale. Gilman (1975) refers to these modes as *polar convective modes*. In the absence of the region outside the tangent cylinder the two polar regions would be disconnected and there would be no preference for either equatorially symmetric or antisymmetric modes; if we consider the outer continuation of this mode, then the Roberts mode, which aligns with the meridional circulation in Figure 20a, will be slightly preferable at onset (Sakuraba, 2002).

The critical radius for thermal Rossby waves will be outside the tangent cylinder, where heat from the inner core can be transported radially at the equator; these modes also peak in amplitude at the equator hence Gilman (1975) refers to these as *equatorial modes*. These will onset before the polar mode for the reasons already discussed.

An equatorial mode will significantly suppress other equatorial modes (of either symmetry), leading to strongly columnar states just above the onset of convection (Figure 1a). However, the polar modes might be expected to onset almost independently (Gilman, 1975) - particularly if the inner core is large. The nonlinear terms of the momentum equation will preserve equatorial symmetry (but not antisymmetry); hence, the onset of these polar modes is important in breaking the equatorial symmetry of the onset state (Figure 1b).

Effect of a magnetic field Fearn (1979) shows that a toroidal field can destabilise the system so

that convection occurs at a lower critical Rayleigh number, provided the magnetic field strength is large enough. The most unstable modes in this case are modes with Busse symmetry which are either modified Rossby modes or magnetostrophic modes when Λ is sufficiently large. Sakuraba (2002) investigates the effect of an axial magnetic field and shows that the polar convective mode can be destabilised at much smaller Λ (in fact, Sakuraba finds that an antisymmetric mode can sometimes be the preferred mode of convection).

In conclusion, we use the terms equatorial and polar modes to describe the modes which peak in amplitude at the respective locations; the most unstable modes in each class are equatorially symmetric and antisymmetric respectively. One cause of confusion is that the magnetic field is a pseudovector, and hence magnetic field lines have the opposite symmetry to the flow.

References

- Aubert, J. 2005, *Journal of Fluid Mechanics*, 542, 53
- Busse, F. H. 1970, *Journal of Fluid Mechanics*, 44, 441
- . 2002, *Physics of fluids*, 14, 1301
- Chandrasekhar, S. 1961, *Hydrodynamic and Hydromagnetic Stability* (Dover Publications, New York)
- Christensen, U. R. 2010, *Space science reviews*, 152, 565
- Dormy, E. 2016, *Journal of Fluid Mechanics*, 789, 500–513, doi: 10.1017/jfm.2015.747
- . 2025, *Annual Review of Fluid Mechanics*
- Dormy, E., Oruba, L., & Petitdemange, L. 2018, *Fluid Dynamics Research*, 50, 011415
- Dormy, E., & Soward, A. M. 2007, *Mathematical aspects of natural dynamos* (Chapman and Hall/CRC)
- Fearn, D. R. 1979, *Geophysical & Astrophysical Fluid Dynamics*, 14, 103
- Feudel, F., Seehafer, N., Tuckerman, L. S., & Gellert, M. 2013, *Physical Review E—Statistical, Nonlinear, and Soft Matter Physics*, 87, 023021
- Feudel, F., Tuckerman, L. S., Zaks, M., & Hollerbach, R. 2017, *Physical Review Fluids*, 2, 053902
- Gastine, T., & Aurnou, J. M. 2023, *Journal of Fluid Mechanics*, 954, R1
- Gastine, T., Wicht, J., & Aubert, J. 2016, *Journal of Fluid Mechanics*, 808, 690
- Gillet, N., & Jones, C. A. 2006, *Journal of Fluid Mechanics*, 554, 343
- Gilman, P. A. 1975, *Journal of Atmospheric Sciences*, 32, 1331
- . 1977, *Geophysical & Astrophysical Fluid Dynamics*, 8, 93
- Guseva, A., Petitdemange, L., & Tobias, S. M. 2025, *Journal of Geophysical Research: Planets*, 130, e2024JE008496
- Hughes, D. W., & Cattaneo, F. 2019, *Journal of Fluid Mechanics*, 879, 793
- Jones, C. A. 2011, *Annual Review of Fluid Mechanics*, 43, 583
- Jones, C. A., Mussa, A. I., & Worland, S. J. 2003, *Proceedings of the Royal Society of London. Series A: Mathematical, Physical and Engineering Sciences*, 459, 773
- Jones, C. A., & Tsang, Y.-K. 2025, *Physics of the Earth and Planetary Interiors*, 360, 107303
- Mason, S. J., Guervilly, C., & Sarson, G. R. 2022, *Geophysical & Astrophysical Fluid Dynamics*, 116, 458
- Menu, M. D., Petitdemange, L., & Galtier, S. 2020, *Physics of the Earth and Planetary Interiors*, 307, 106542
- Oruba, L., & Dormy, E. 2014, *Geophysical Journal International*, 198, 828, doi: 10.1093/gji/ggu159
- Roberts, P. H. 1968, *Philosophical Transactions of the Royal Society of London. Series A, Mathematical and Physical Sciences*, 263, 93

- Roberts, P. H., & Soward, A. M. 1992, *Annual Review of Fluid Mechanics*, 24, 459, doi: <https://doi.org/10.1146/annurev.fl.24.010192.002331>
- Sakuraba, A. 2002, *Geophysical & Astrophysical Fluid Dynamics*, 96, 291
- . 2007, *Journal of Fluid Mechanics*, 573, 89
- Sánchez, J., Garcia, F., & Net, M. 2013, *Physical Review E—Statistical, Nonlinear, and Soft Matter Physics*, 87, 033014
- Seeley, W., Coke, F., Simatev, R., & Teed, R. 2025, *Fluids*, 10, doi: [10.3390/fluids10090237](https://doi.org/10.3390/fluids10090237)
- Simatev, R., & Busse, F. H. 2003, *New Journal of Physics*, 5, 97
- Simatev, R. D., & Busse, F. H. 2009, *Europhysics Letters*, 85, 19001
- Skene, C. S., Marcotte, F., & Tobias, S. M. 2024, arXiv preprint [arXiv:2411.05499](https://arxiv.org/abs/2411.05499)
- Soderlund, K. M., King, E. M., & Aurnou, J. M. 2012, *Earth and Planetary Science Letters*, 333, 9
- Sreenivasan, B., & Jones, C. A. 2006, *Geophysical Journal International*, 164, 467
- Teed, R. J., & Dormy, E. 2023, *Journal of Fluid Mechanics*, 964, A26
- . 2025a, *Geophysical Research Letters*, 52, e2025GL118078
- . 2025b, *Physical Review Fluids*, 10, 103702
- Tobias, S. M. 2021, *Journal of fluid mechanics*, 912, P1